GRADUATE AERONAUTICAL LABORATORIES
CALIFORNIA INSTITUTE OF TECHNOLOGY

Shock Wave Processing of Transitional Metal Silicides

Karina L. Montilla

1997

Firestone Flight Sciences Laboratory

Guggenheim Aeronautical Laboratory

Karman Laboratory of Fluid Mechanics and Jet Propulsion

Pasadena

Shock Wave Processing of Transitional Metal Silicides

Thesis by
Karina L. Montilla

In Partial Fulfillment of the Requirements
for the Degree of
Doctor of Philosophy

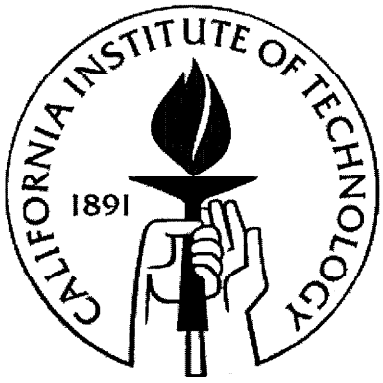

California Institute of Technology
Pasadena, California
1998
(Submitted September 11, 1997)

Throughout the years, I have had the opportunity to interact with brilliant professors who have enlightened me on numerous subjects: Profs. Wolfgang Knauss; Ares Rosakis; Michael Ortiz; Kaushik Bhattacharya; James Knowles; Bill Johnson; and Brent Fultz; all of whom have given their time freely toward my academic enrichment. At the University of Rhode Island, I

am deeply indebted to Professors Frank White and Arun Shukla for their support and encouragement in my pursuit of a graduate degree.

My years at Caltech have been greatly enhanced by all the great friends that I have made. I have met so many wonderful, interesting individuals that I could not attempt to name them all. A few people deserve special recognition: Dr. Danny Howard, the first African-American to graduate from the Graduate Aeronautical Laboratories at Caltech. Danny was not only instrumental in my making the decision to attend Caltech, but for making sure I had the right tools to finish; Douglas Varela, the eternal graduate student, for never letting me quit; on a more personal note, I must thank my fashion-conscious ex-roommate, Marilena, for making my first two years at Caltech the most memorable; my worldly Norwegian/German/Venezuelan friend, Anne (a.k.a. Helga), for making the last three so much fun! And of course, there are those friends that go back to my first week at Caltech: Pin, Roberto, Phil, Miltos just to name a few.

I extend heartfelt thanks to my loving family and husband. John, I will never forget the incredible sacrifice you have made for me so that I may finish my degree while putting yours on hold. I hope that I can make it up to you one day; my hardworking parents for leading exemplary lives and being wonderful role models; and for leaving their friends, family and beautiful homeland behind to give me and my sisters the awesome opportunity to live and study in the greatest country in the world.

Lastly, I would like to acknowledge the financial support of the Irvine Foundation for my fellowship and the National Science Foundation.

ABSTRACT:

Shock wave consolidation is an innovative processing technique for the densification of initially porous media. A compressive shock wave is introduced in the material by the impact of a high velocity flyer plate. Densification is achieved via intense inhomogeneous plastic deformation, pore collapse, and localized melting around particle surface. The passage of the shock wave may also induce chemical reactions within the material. The chemical reactivity of the powders are enhanced through dislocation nucleation, plastic flow, grain fracture and mass mixing as a result of the shock wave.

A systematic investigation is performed to examine the effects of particle size and porosity on the initiation of the Ti_5Si_3 reaction from the elemental powder mixture (i.e., 5 Ti + 3 Si). The initial powder porosity is varied from 40% to 49% of the theoretical density for two different size powders. The threshold shock energy necessary for complete silicide reaction is established. The powders are consolidated with shock energies up to 671 J/g and shock pressures up to 7.3 GPa. The threshold shock energy for the large powder mixture is found to be approximately 80% higher than that for the smaller powder mixture. For both sized powders, an increase in the

threshold shock energy of 75% is observed in decreasing the initial porosity of the powders from 49% to 40%. Evidence for the reaction of solid Ti and liquid Si is observed in isolated regions at shock energies slightly below the threshold energy.

Mechanical alloying and shock wave consolidation are examined as viable alternatives for the synthesis and consolidation of $MoSi_2$. Mechanical alloying of Mo + 2Si is monitored with X-ray diffraction and differential scanning calorimetry (DSC). The milling time is varied from two hours to one hundred forty-four hours. Nanocrystalline $MoSi_2$ is observed after sixteen hours of ball milling. X-ray diffraction is used to follow the extent of alloying and average grain size as a function of ball milling time. DSC is utilized to determine the onset endothermic and exothermic reactions in the ball milled powder. $MoSi_2$ is produced from the elemental powder mixture by shock wave consolidation.

TABLE OF CONTENTS

LIST OF FIGURES

LIST OF TABLES

Chapter 1. Introduction

The main objective of this investigation is to bring to light the underlying mechanisms controlling shock-initiated chemical reactions in solids. There is a wide range of materials for which shock consolidation is a viable processing technique, the focus of this study is silicide formation of transitional metals. Silicides of transition metals are of great interest due to their high melting point, high thermal conductivities and excellent oxidation resistance [1-4]. In addition to these properties, their high thermal stability, low electrical resistivity, and exceptional diffusion-barrier characteristics make silicides an attractive option for microelectronics applications [4].

Engine manufacturers have conducted studies which show that intermetallics can yield significant payoffs in terms of strength-to-weight ratio, fuel efficiency, and direct operational cost [2]. They envision a 20% improvement in fuel efficiency. The savings would be achieved through a reduction in the specific fuel consumption of the engine depending on the specific engine and the material used. Silicides are intermetallics that perform well under extended high temperature-applications (i.e., retention of strength at high temperatures). Thus, the aerospace industry has a great deal to gain if these advanced high temperature materials can be successfully processed. Silicides offer a significant weight advantage over currently used

Ni-based superalloys in high temperature applications. For the last few decades, silicides have been used as thermally and electrically conducting materials for a wide range of applications including as heat shields for rocket engines and commercial heating elements [3]. Silicides are unique in their ability to provide a silica layer upon high temperature oxidation. This property is the subject of an extensive exploration of protective silicide based coatings for the refractory metals which have poor oxidation resistance.

1.1 Background

Shock wave consolidation is an innovative processing technique for the densification of an initially porous media. A compressive shock wave is introduced by a high velocity impact of a flyer plate onto a green compact. A well bonded solid is attained via intense inhomogeneous plastic deformation, pore collapse and localized melting around particle surface [7-9]. This is a highly dynamic process which occurs during a microsecond scale time duration of high pressure, stress, strain-rate and temperature state [8]. Due to its short processing time and preferential energy deposition on the particle surface, the temperature of the bulk solid remains relatively low. The result is a well bonded solid with minimal microstructural modifications [7-9]. Shock wave consolidation also offers the capability of producing both equilibrium and non-equilibrium microstructures. The high rate of loading and high pressures associated with shock wave processes are not attainable by any other method.

Shock initiated reaction synthesis is a process where chemical reactions are initiated within the powder by the passage of a shock wave. The chemical reactivity of the powders are enhanced via dislocation nucleation, plastic flow, grain fracture and mass mixing as a result of the shock wave. These factors lead to unusually high rates of chemical reactions. Figure 1.1 is a schematic representation of the parameters associated with shock wave processing leading to enhanced chemical reactivity. Radiation pyrometry measurements have shown that strong chemical reactions in an aluminum-nickel mixture are induced in a 100 nanosecond time scale during shock compression [6].

Shock wave consolidation is normally performed by one of two methods, consolidation by impact of a flyer plate or detonating explosives attached to the specific geometry (i.e. hollow cylinder). Explosive detonations offer the advantage of net-shape processing and larger component capabilities. However, flyer impact geometry offers greater control of the shock consolidation parameters and improved sample recovery. Thus, for investigation of shock-initiated chemical reactions the flyer impact method is extensively used with the exception of studies on the role of shear bands in reaction initiation [10-12].

1.2 History of Reactions Synthesis

After World War II many ordinance laboratories around the world were able to convert technology developed for weapons into technology for the investigation of matter under explosive loading. The foresight for this

new field of study is attributed to the visionary work of Rice, Walsh and McQueen of Los Alamos Laboratory [13]. With this new technology, materials could be loaded in an explosive manner with reproducible results. It is during these early studies that shock initiated chemical reactions are first observed.

High pressure shock initiated chemical reactions have been documented as early as the mid-nineteen fifties by Riabinin in Russia, who documented the decomposition of magnesium carbonate to a mixture of magnesium oxide and carbon dioxide [14]. In the U.S., DeCarli and Jamieson brought shock compression synthesis to the forefront through their work on diamond formation (particles < 10 μm) by explosive shock synthesis [15]. Subsequently, the enhanced sinterability of shock-modified ceramic powders, shock induced cross linking and polymerization are observed [14-16]. A number of studies where also being conducted in Japan in the sixties [17,18]. Prior to the last several decades, there was very little research on shock-initiated chemical reactions with the exception of Batsanov and co-workers in the Soviet Union [19,20]. Batsanov et al. observed the decomposition of a number of carbonates, sulfates and nitrates.

A comprehensive shock-synthesis research effort initiated in the eighties by Graham and co-workers [13,14] has flourished with work by Boslough [6,21], Vreeland et al. [23-25], Meyers et al. [10-12,22], and Thadhani et al. [7,26-27]. The extremely dynamic, irreversible nature of shock compaction and short duration makes it extremely difficult to measure the parameters

needed to model the process. In spite of the many advances in probes to measure the mechanical and thermal response, most investigations rely heavily on the recovery of the sample for reaction characterization. Thus, shock initiated chemical reactions remain poorly understood. At present, there is no generally accepted theory which defines the threshold condition for initiation or the reaction kinetics of the process. In fact, there is some controversy as to when and how the chemical reactions take place. From post-shock microstructural evaluation, it is difficult to determine if these reactions occur within the shock front or after its passage. There are also conflicting views as to whether these are solid-solid or solid-liquid state reactions. Some of the mechanistic models describing the process are presented in section 2.3.

1.3 Outline of Work

This thesis is organized into four independent chapters. Chapter 2 provides the reader with an elementary review of shock wave physics and the mathematical formulation of shock waves in a porous media. Mechanistic models describing the shock consolidation process are also presented. Chapter 3 describes a study performed to determined the threshold shock energy required for the Ti_5Si_3 reaction in elemental powders. The threshold shock energy is defined as the minimum amount of energy required for complete reaction between the elemental powders. The effects of initial porosity and powder size are established. The porosity is varied from 40% to 49% for two different powder sizes.

Chapter 4 presents a study on grain size refinement and alloying via mechanical ball milling of Mo + 2 Si elemental powder mixture. The ball milling time is increased from two hours to one hundred and forty-four hours, and the grain size is monitored using X-ray diffraction and transmission electron microscopy. Differential scanning calorimetry is used to monitor the onset of endothermic and exothermic reactions within the powder as a function of ball milling time. The as-received powder is shock consolidated to produce $MoSi_2$. The recovered compacts are sectioned and examined by optical microscopy and scanning electron microscopy.

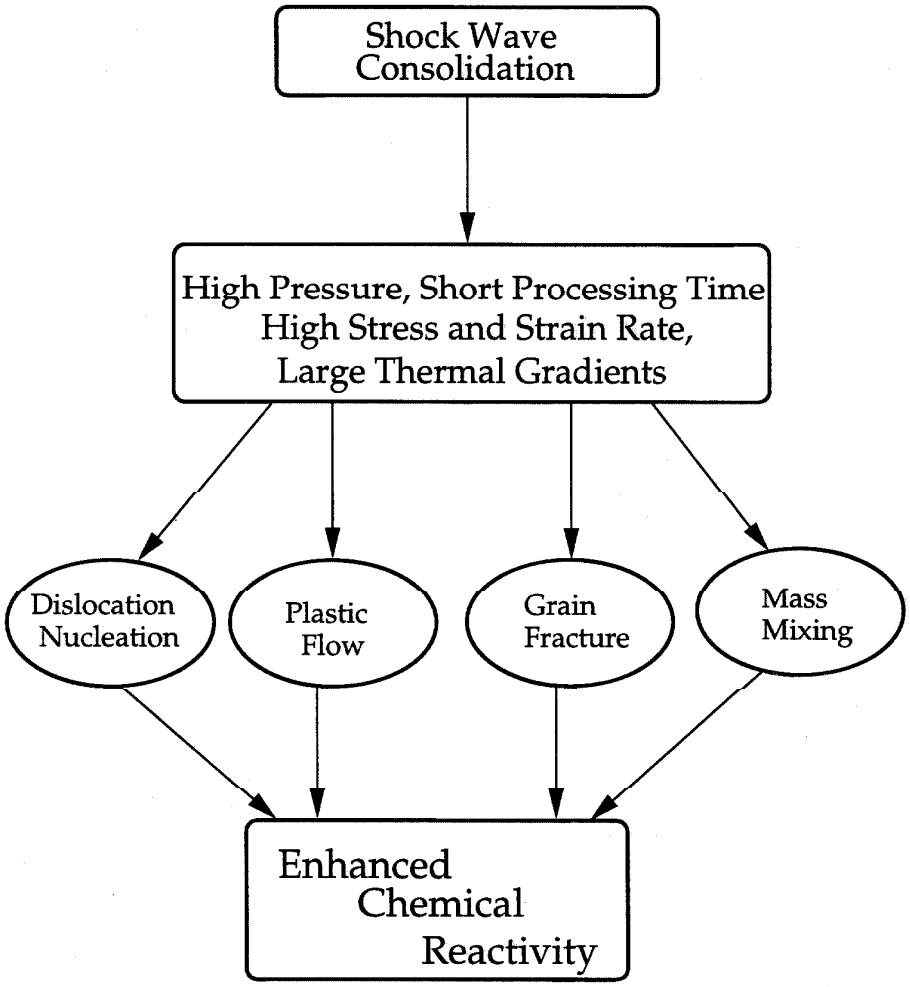

Figure 1.1 Schematic representation of shock processes leading to enhanced chemical reactivity.

References:

1. Z.A. Munir, *Ceram. Bull.*, **67**, p. 324 (1988).

2. A.K. Vasudevan, J.J. Petrovic, *Mat. Sci. and Eng.*,**A155**, p. 1 (1992).

3. R.B. Shwarz, S. R. Srinvasan, J.J. Petrovic and C.J. Maggiore, *Mat. Sci. and Eng.*, **A155**, p. 75 (1992).

4. D. M. Shah, D. Berczik, D.L. Anton and R. Hecht, *Mat. Sci. and Eng.*, **A155**, p. 45 (1992).

5. R.Radharkrishnan, S. Bhaduri, and C.H. Henager,Jr., *JOM*, **1**, p. 41 (1997).

6. M. B. Boslough ,*Chem. Phys. Lett.*, **160**, p. 618 (1989).

7. N.N. Thadhani, *Prog. Mat. Sci.*, **37**, p. 118 (1993).

8. H.W. Goudin, *Prog. Mat Sci.*, **30**, p. 39 (1996).

9. D. Raybould, J. Mat. Sci., **16**, p. 589 (1981).

10. V.F. Nesterenko, M.A. Meyers, H.C. Chen, and J.C. LaSalvia, *Shock Compression of Condensed Matter Conference*, Seattle, Washington, August 13-18, 1995.

11. K.S. Vecchio, L.-H. Yu, M.A. Meyers, *Acta Metall. Mater.*, **42** (3), p. 701 (1994).

12. V. F. Nesterenko, M.A. Meyers, H.C. Chen, J.C. LaSalvia, *Appl. Phys. Lett.*, **65**, p. 3069 (1994).

13. R.A. Graham, "*Solids Under High-Pressure Shock Compression*," Springer-Verlag (1993).

14. R.A. Graham, B. Morosin, B. Dodson, "*The Chemistry of Shock Compression: A Bibliograpy*, " Sandia Report (1983).

15. P.S. DeCarli and D.J. Milton, *Science*, **174**, p. 144 (1965).

16. O.R. Bergmann and J. Barrington, *J. Amer. Cer. Soc.*, **49**, p. 502 (1966).

17. H. Suzuki, H. Yoshida, Y. Kimura, *J. Ceramic Assoc. Japan*, **77**, p. 36 (1969).

18. Y. Kimura, *Japan J. Appl. Phys.*, **2**, p. 312 (1963).

19. S.S. Batsano, *Russian Chem. Rev.*, **37**, p. 197 (1968).

20. S.S. Batsanov, "*Synthesis Under Shock-Wave Pressure*", in Preparative Methods in Solid State Chemistry, Academic Press, NY, p. 133 (1972).

21. M. B. Boslough, *Rev. Sci. Instrum.*, **60**, p. 3711 (1989).

22. M.A. Meyers, S.S. Batsavov, S.M. Gavrilkin, H.C. Chen, J.C. LaSalvia, F.D.S. Marquis, *Mat. Sci. and Eng.*, **A201**, p. 150 (1995).

23. R. B. Schwarz, P. Kasiraj, T. Vreeland Jr. and T.J. Ahrens, *Acta Metall.*, **32**, p. 1235 (1984).

24. B.R. Krueger and T. Vreeland,Jr, *J. Appl. Phys.*, **69** (2), p. 720 (1991).

25. B.R. Krueger, A.H. Mutz and T. Vreeland, Jr., *Met. Trans.*, **23A**, p. 55 (1992).

26. N.N. Thadhani, *J. Appl. Phys.*, **76**, p. 2129 (1994).

27. N.N. Thadhani, S. Work, R. A Graham and W. F. Hammetter, *J. Mater. Res.*, **7**, p. 1063 (1992).

Chapter 2. Shock Wave Consolidation

An elementary description of shock wave physics is presented in this chapter to enable the reader to follow and interpret the experimental results. First, the mathematical formulation of shock waves in a porous media is presented, followed by the model developed by Schwartz et al. which describes the consolidation process [1]. In this chapter, the reader is also introduced to the mechanistic models that have been proposed to describe shock consolidation and the processes that may lead to enhanced chemical reactivity. This chapter will furnish the reader with the fundamental background to appreciate the complexity of the shock consolidation process.

2.1 Shock Waves in Porous Media

A shock wave is a discontinuity in pressure, density and internal energy across a media. Figure 2.1 illustrates the state of the material before and after the passage of a plane shock wave. Where U_p, Us, ρ, P, E are the particle velocity, shock velocity, density, pressure and specific internal energy, respectively. The subscript zero (o) refers to the initial state. In our case, the stress wave is introduced onto the porous media by a flyer plate impact.

A mathematical description of the shock wave in a porous media can be obtained using conservation of mass, momentum and energy. This is the same formulation first developed by Rankine and Hugoniot for shock waves

in fluids. For a well defined shock front propagating at constant speed into a medium under rest in the absence of chemical reactions, the conservation equation for mass, momentum and energy flux across the shock are [2]:

$$(U_s - U_p)\rho = U_s\rho_o \tag{2.1}$$

$$U_p(U_s - U_p)\rho = P - P_o \tag{2.2}$$

$$U_pP = \rho E(U_s - U_p) + \tfrac{1}{2}\rho U_p^{\,2}(U_s - U_p) - \rho_o E_o U_s \tag{2.3}$$

We can combine equations 2.1 and 2.2 and rewrite equation 2.3:

$$P - P_o = \rho_o U_s U_p \tag{2.4}$$

$$(E - E_o) = \frac{1}{2}(P + P_o)(V_o - V) \tag{2.5}$$

where, V is the specific volume $(1/\rho)$. This results in three equations with four unknowns, so an additional relationship is required to calculate the state behind the shock. Often, this additional relationship is one that relates the shock pressure to the particle velocity. This relationship is known as the Hugoniot of the material. It is usually obtained experimentally by measuring the velocity at which a shock wave, generated by the impact of a flyer plate of known material properties, propagates in the media. Fortunately, Hugoniot data for most materials of structural interest have been determined and are tabulated [3]. The remaining shock parameters in the conservation equations can now be calculated using the Hugoniot data.

The fundamental theory for shock Hugoniot in porous media was published in nineteen sixty-six by Zeldovick and Raizer[4]. However, a much simpler but accurate analytical model for the Hugoniot relationship in porous media was derived by Simons and Legner in the early eighties [5]. The model predicts the Hugoniot of the porous media from that of its solid counterpart. From the density of the material, distension ($m = V/V_O$) of the powder, isentropic compressibility (κ) and the Gruneison coefficient (γ), the model calculates the particle velocity as a function of shock pressure [6]:

$$U_p^2 = \frac{P}{\rho_o}\frac{m(1+P\kappa)-1}{1+(1+\frac{\gamma}{2})P\kappa} \tag{2.6}$$

where, the Gruneisen coefficient (γ) is:

$$\gamma = V(\frac{\partial P}{\partial E})\Big|_v \tag{2.7}$$

A program which employs the Simons and Legner model to solve for the particle velocity was written by A.H. Mutz [6]. The program also employs the method of impedance matching to solve for the Hugoniot of the different powder mixtures. The method of impedance matching is often used to calculate the unknown Hugoniot of a material from the known Hugoniot of another material as previously mentioned by measuring the propagation velocity of an induced shock wave by a flyer plate.

This method can be described graphically. Figure 2.2 depicts a flyer plate traveling at U_f impacting a target, of known Hugoniot, at rest. Shock waves originating at the interface will propagate into both the flyer plate and

target [2]. Since both the material velocity and stress must be continuous across the interface, it is advantageous to work in the pressure versus the material velocity plane. Since the target is initially at rest, its origin is at U_f = 0 with a corresponding positive slope. The state behind the shock is given by the known Hugoniot of the flyer plate material. From the conservation of momentum equation, we can calculate the shock speed in the target from the thickness of the flyer plate and the transit time of the shock. It follows that the slope of a straight line joining the final state with the origin is $U_s\rho_o$. So that, the acoustic impedance ($U_s\rho_o$) of the target is matched to that of the flyer.

The passage of a shock wave through a porous media is significantly more complex than one traveling in a solid largely due to the non-uniform plastic deformation. In addition, the energy deposited in the powder is always greater than the energy deposited in a solid target under the same ~~conditions~~ pressure. The energy discrepancy can be seen from the Hugoniot of a hypothetical porous material in the pressure-volume plane. From Figure 2.3, one can see that for a given stress level the net energy is much larger for the porous material than a solid [7]. The diagram shows a porous media at an initial specific volume V_o being shock consolidated to a volume V by a single shock wave of amplitude P_s. V_o is generally much larger than the corresponding solid volume. Thus, at a given stress level (P) the specific energy deposited in the porous media is much larger than in the solid. One of the results of the increased energy deposition is a much greater temperature increase in porous media compared to that of a solid under similar shock condition.

2.2 Physics of Shock Consolidation

The shock wave consolidation process can be visualized as several distinct processes. Schwarz et al. proposed a theory for the shock-wave consolidation of powders which models the entire process [1]. The following is a brief summary of the process as presented by Schwarz. Each step in the process is characterized by the time constant corresponding to its duration.

The first step is densification and surface melting which occurs within the shock front. The shock rise time is on the order of the particle diameter divided by the shock velocity. Densification is followed by solidification of the melted region. This time is difficult to calculate since neither the size nor the shape of the melted region in known a priori. An estimate of the initial mass fraction melted and the temperature of the unmelted region in the shocked state was used. Post-shock experiments reveal that initially spherical particles deform to oblate spheroids so, they are modeled as a box with sides d, d, d/2 (d= diameter of particle) in 2-D. If uniform melting is assumed around the particle, it will be surrounded by a molten layer h=Ld/4, where L is the mass fraction of the melt. Since melting is not uniform, the worst case is that all the melting is on one side so that h=Ld. Assuming the thickness of the melt is much smaller than the particle diameter, the problem can be approximated by that of the solidification of a slab of thickness h/2 in contact with a semi-infinite solid at the initial temperature T. For a fixed liquid-solid interface and no superheating of the melt, the solidification time is [1]:

$$t_s = \frac{\pi D_m}{16}\left[\frac{Ld\,H_m\rho}{K_m(T_m - T)}\right]^2 \tag{2.8}$$

$$D_m = \frac{K_m}{\rho\, C_{p,m}} \tag{2.9}$$

where K_m is the thermal conductivity, D_m is the diffusivity at the melting temperature, $C_{p,m}$ is the specific heat at the melting temperature, H_m is the latent heat of fusion, and T_m the melting temperature. For an iron particle with a diameter of 58 μm, this time constant is approximately 200 ns.

After solidification, the compact exhibits a heterogeneous temperature profile. Thermal relaxation to a homogenous temperature is the next step. The homogenous temperature T_h is in the order of $x^2/4D_m$, where x is a characteristic distance of the initial temperature distribution. Taking x to be about a quarter of the particle diameter, the calculated time constant is t_h= 10 μs. This is much longer than the shocked state of these experiments (~2 μm), thus the homogenous temperature is achieved in the unloaded state. The temperature within the sample will be reduced further to the ambient temperature, t_a. It is in the order of $t_h(1/d)2$, where 1 is the smallest dimension of the compact. The final and most important time constant that is required is the duration of shock state which is easily controlled from the experimental variables (i.e. flyer plate thickness). Table 2.1 is a summary of these important time constants.

Dynamic pore collapse in porous materials also plays an important role in the shock consolidation process. Tong and Ravichandran studied the effects of dynamic loading rate, pore size, strain-rate sensitivity, strain hardening, thermal softening and initial porosity on the pore collapse process leading to consolidation [8]. The finite deformation of an elastic/viscoplastic spherical shell under impulsive pressure loading was analyzed. The typical pressure rate is on the order of 1-100 Mpa/ns or higher (i.e., for shock pressures of 1-10 Gpa and shock rise times of 100-1000 ns). They found that the pore size plays a major role in the shock rise time and hence, on the consolidation process [8,9]. The implications of their finding on our experimental results are discussed in Chapter 3.

2.3 Mechanistic Models

There have been a number of mechanistic models introduced to explain the chemical reactions and structural changes occurring during the submicron time duration of shock compression. This section introduces the models that will be referenced in the following chapters.

2.3.1 Roller Model

One of the first models to describe the governing mechanism of shock initiated chemical reaction is the ROLLER model proposed by Dremin and Breusov [10]. The model represents a chemical process in the presence of plastic flow. A schematic representation of the Roller Model is illustrated in Figure 2.4. It illustrates the decomposition of a compound AB and the formation of a phase AB. Dremin and Breusov assert that when two layers

of a substance are displaced relative to one another, the nuclei of phase A, located between them, can be regarded as a kind of roller about which alloying and mixing of the components take place. Since the time required for the rearrangement of electron shells (10^{-13} - 10^{-14} s) is much shorter than the time required for contact between atoms, it follows that all the atoms 'A' passing in the immediate vicinity of the nucleus have sufficient time to combine with the substance (growth of the nuclei of the new phase).

In the growth of new-phase nuclei behind the shock-wave front, the entire mass of the initial phase is transported by the plastic flow in the vicinity of the crystallization centers and the required atoms combine selectively with the particles of the new phase undergoing continuous growth during this process. This process is quite different from the usual diffusional growth of crystallization center, in which each atom must find its way to the new phase, pushing apart its neighbors.

2.3.2 The VIR Model

A conceptual model of the chemical changes occurring during shock synthesis was developed by Horie et. al [11] . The model attempts to differentiate between the effects of high shock pressure and high strain rate to those of the high temperature on the macroscopic behavior of porous reactive powder mixtures. Since the bulk pressure and temperature are interrelated, this can be difficult, but, they observe a distinct temperature signature (i.e. a threhold shock-initiated temperature above which reactions

occur). The features of the observed chemical changes in the binary Ni-Al system can be summarized as follows:

$$A + B \rightarrow (A_xB) \rightarrow A_3B$$

An intermediate state of a nonequilibrium mixture of A and B is a result of dispersive macromixing of particles, mixing due to interfacial instability, and microscopic diffusion. The next step represents the formation of a final product. Figure 2.5 is an illustration of the model in one dimensional spatial coordinates. The initial configuration is a triple-layered slab with a void between the two constituent elements. As the shock travels from left to right, it triggers the collapse of the void and the formation of the nonequilibrium mixture. The final step is the chemical reaction initiation resulting in the bulk product. The mathematical formulation of the process applies the conservation of mass of each of the chemical species.

This model evolved to a simplified mathematical model known as the VIR (Void, Inert and Reactive) model, shown in figure 2.6. Similar to the slab configuration, the heterogeneous mixture of voids, inert species, and reactant species are in pressure equilibrium, but not thermal equilibrium. The inert species plays a major role in the quenching of the reaction, since heat flow generally occurs from the reactive species to the inert species and voids.

2.3.3 The CONMAH Model

The CONMAH (configuration change, mixing, activation, and heating) model proposed by Graham outlines the processes leading to configuration changes prior to solid-state reaction initiation [12]. A schematic

representation of the parallel plates whose spacing is changed by the shock deformation process is illustrated in Figure 2.7. The shock is moving from the bottom to the top. The process is divided into three sequential parts, an initial configuration; a transition zone; and a final compressed configuration. The initial configuration which encompass powder morphology and porosity is crucial in energy localization, mass mixing and fluid-like flow. The next regime, transition zone, is one of peak rise in pressure with a time constant in the order of nanoseconds. The last step is the unloading of the solid to ambient pressure. This model has been found to be consistent with experimental results [7,11,12].

Table 2.1 Characteristic time constant in shock consolidation

Process	Typical Value
Densification and melting	40 ns
Solidification of molten region	200 ns
Thermal relaxation to homogeneous temperature	10 μs
Thermal relaxation to ambient temperature	≥ 5 ms
Duration of shocked state	2 μs

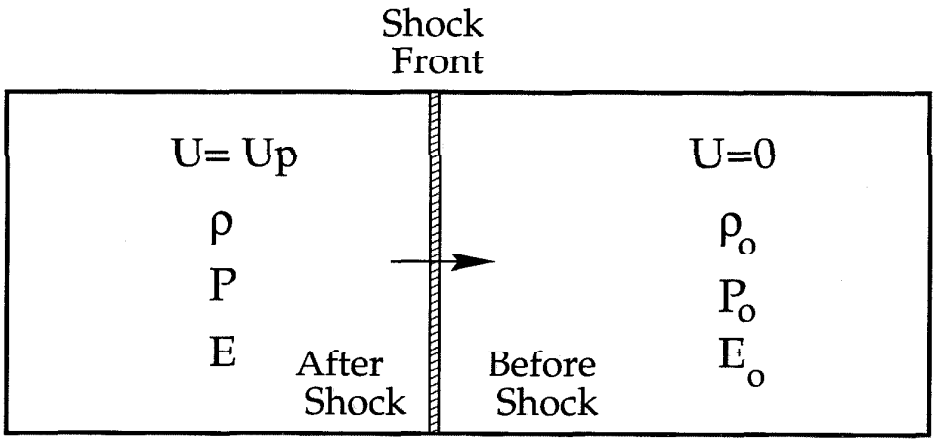

Figure 2.1 Schematic of plane shock front.

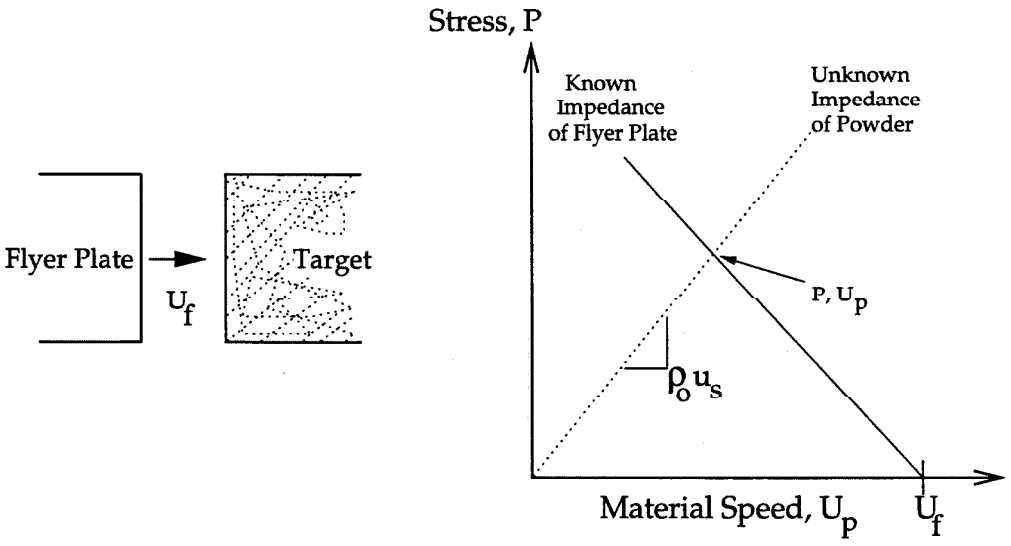

Figure 2.2 Impedance matching for Hugoniot determination

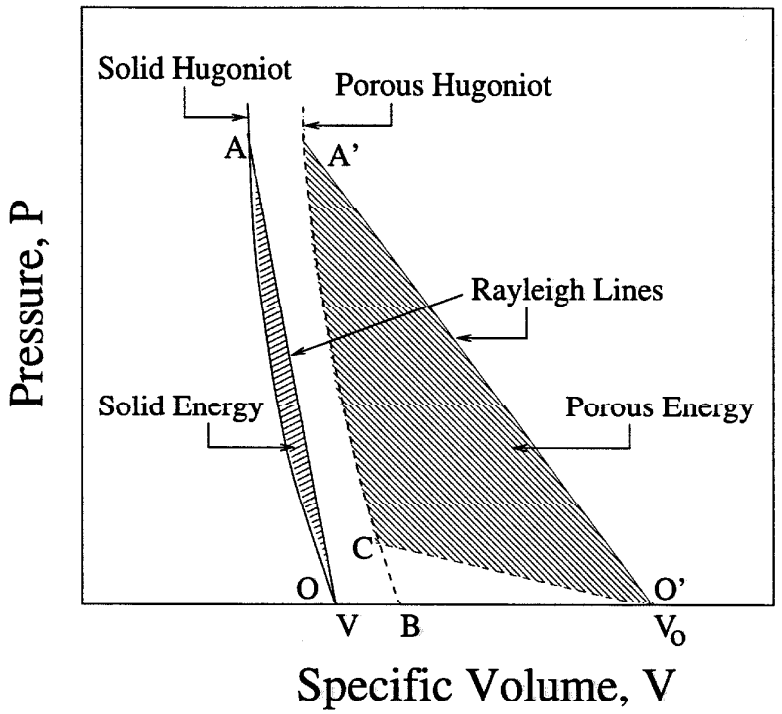

Figure 2.3 Comparison of P-V Hugoniot for solid and porous media. Curves O'BA and O'CA' are for typical metal powders and curve OA is for a solid density material [7].

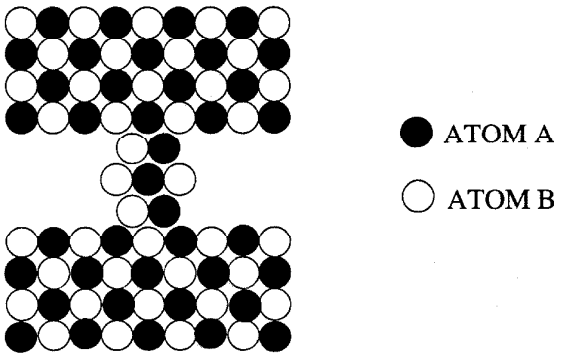

(a) Decompositon of Compound AB

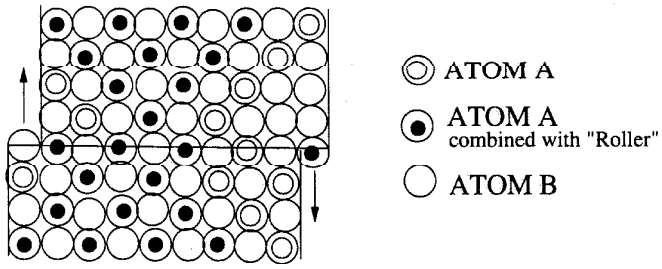

(b) Growth of Phase AB

Figure 2.4 Schematic of the Roller Model

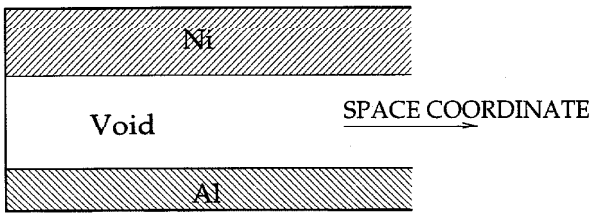

a. Initial State

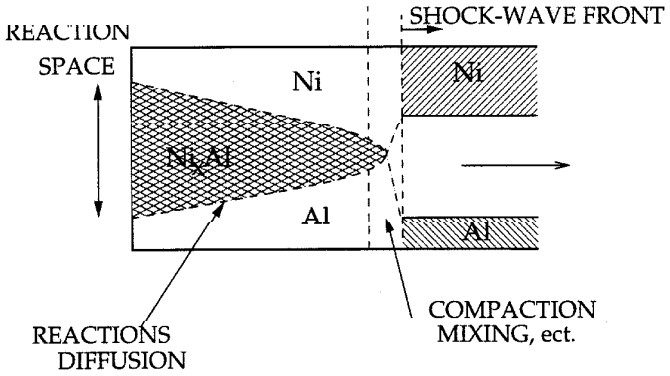

b. Shocked State

Figure 2.5 Model for chemical reactions in a binary powder [11].

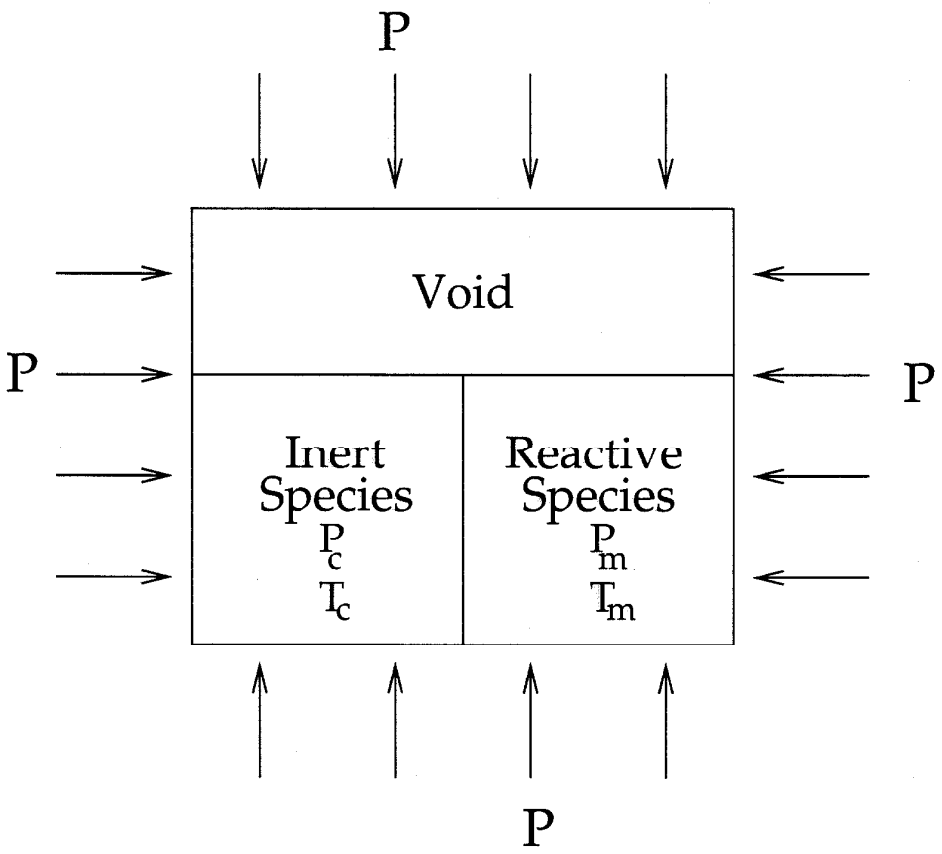

Figure 2.6 The VIR Model
(Void, Inert Species and Reactive Species)

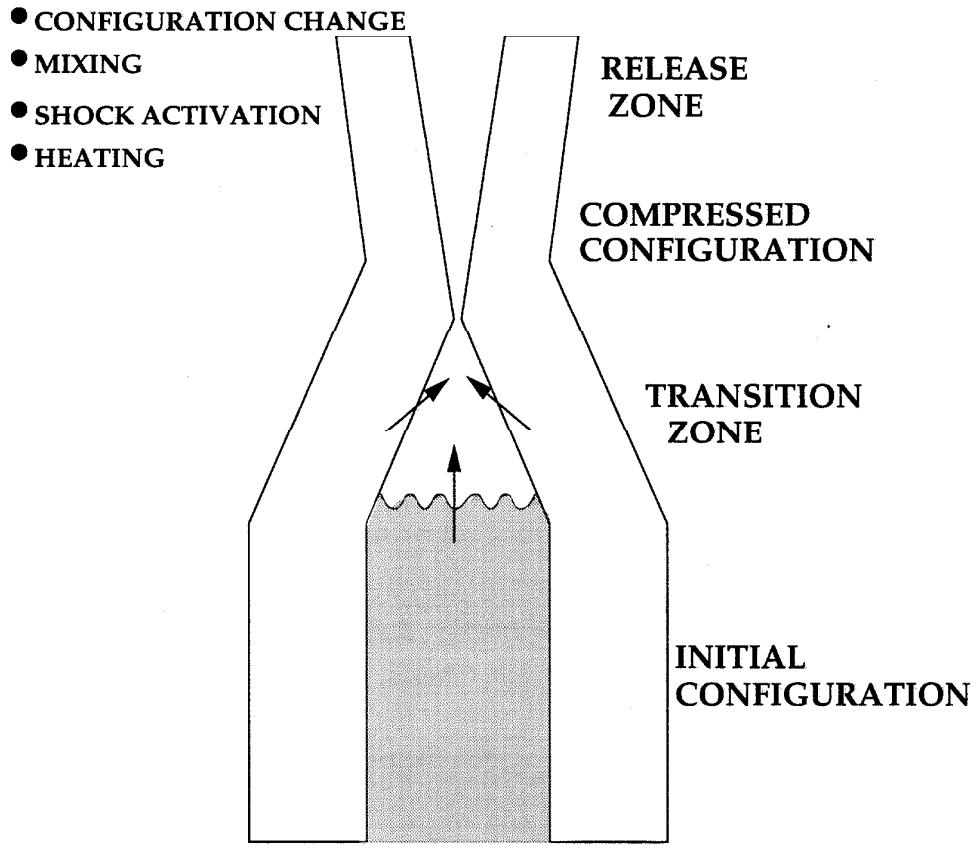

Figure 2.7 CONMAH Model
Schematic of Processes during
solid-state chemical reactions

References:

1. R. B. Schwarz, P. Kasiraj, T. Vreeland Jr. and T.J. Ahrens, *Acta Metall.* **32,** p. 1235 (1984).

2. H.W. Goudin, *Prog. Mat Sci.*, **30**, p. 39 (1996).

3. S.P. Marsh ed., "LASL Shock Hugoniot Data," University of California Press, Los Angeles, 1980.

4. Y.B. Zel'dovich and Y. P. Raizer, "Physics of Shock Waves and High Temperature Hydrodynamic Phenomena," ed. W.D. Hayes and R.F. Probstein (Academic, New York, 1966).

5. G. Simons and H. Legner, *J. Appl. Phys.* **53**, p. 943 (1982).

6. A. H. Mutz, "*Heterogeneous Shock Energy Deposition in Shock Wave Consolidation of Metal Powders,*" Ph.D. Thesis, Caltech, 1991

7. N.N. Thadhani,*J. Appl. Phys.* **76**, p. 2129 (1994).

8. W. Tong and G. Ravichandran, *J. Appl. Phys.* **74** (4), p. 2425 (1993).

9. W. Tong and G. Ravichandran, *Appl. Phys. Lett.* **65** (22), p. 2783 (1994).

10. A.N. Dremin and O.N. Breunov, *Russian Chem. Rev.* **37**, p. 392 (1968).

11. Y. Horie, M. E. Kipp, *J. Appl. Phys.* **63**, p. 5718 (1988).

12. R.A. Graham, "Solids Under High-Pressure Shock Compression," Springer-Verlag (1992).

13. N.N. Thadhani, S. Work, R. A Graham and W. F. Hammetter, *J. Mater. Res.* **7**, p. 1063 (1992).

CHAPTER 3. Shock Wave Initiation of the Ti_5Si_3 Reaction

The Ti_5Si_3 silicide continues to receive a considerable amount of attention due to its low density, high melting point, and oxidation resistance at elevated temperature [1-4]. These properties, along with high electrical and thermal conductivity, set Ti_5Si_3 above all the other 5:3 silicides. Hence, it is of great interest in a wide range of applications from turbine airfoils to electronic interconnects.

A systematic investigation is performed to examine the effects of particle size and porosity on the initiation of the Ti_5Si_3 reaction from an elemental powder mixture (i.e., 5Ti + 3Si). The initial powder porosity is varied from 40% to 49% of the theoretical density for two different size powders. The threshold shock energy necessary for complete reaction is established. The shock energy is calculated as the work done by the shock upon reducing the porosity to zero:

$$E_s = \tfrac{1}{2}P(V_o - V) \tag{3.1}$$

P is the shock pressure and V_o and V are the initial and final volumes, respectively. These powders are consolidated with shock energies up to 671 J/g and shock pressures up to 7.3 GPa.

3.1 Background

A preliminary study by Krueger et al. found that the condition for shock initiation of the Ti_5Si_3 reaction is sensitive to both initial porosity and residual oxygen in the pores [2]. Experiments are performed both in residual argon and in air atmosphere. The threshold shock energy for the reaction is much lower for those experiments conducted with residual air. This reduction in shock energy is attributed to the large negative heat of formation of titanium oxide, which is believed to trigger the reaction at the lower shock energy. The heat of formation can be as large as -2,460 kJ/mol (for Ti_3O_5).

Dunbar and co-workers investigated the shock loading and subsequent reaction of the 5Ti + 3Si powder mixtures with coarse, medium and fine morphologies [4,5]. A PVDF piezoelectric polymer stress-rate gauge is used to detect and record stress pulses to and propagated through the powder mixture. They found that the coarse morphology powder exhibits a higher threshold for reaction than the medium morphology powder. The fine morphology powder mixture displays a higher than expected threshold for reaction which is attributed to poor mixing between Ti and Si due to particle agglomeration. They assert that these results are consistent with the CONMAH (configurational changes, mixing and heating) conceptual model of shock-induced solid-state chemical process discussed in Chapter 2. Hence, for the fine morphology powder the particle agglomeration inhibits mixing which results in the elimination of a key factor for reaction initiation.

Bordeaux and Yavari place two basic criteria on whether or not exothermic reactions are possible [6]. The first condition is that the heat of the reaction must be sufficiently in excess of that required to form melt in the mixture. The second condition that the mixing reaction time must be much shorter than the time for dissipation of the heat of reaction to the environment. Both conditions are intuitive but can be hard to substantiate for shock consolidation. These conditions are examined in section 3.5.

Recently, Thadhani classifies shock initiated reactions into two categories: shock-induced and shock-assisted solid-state chemical reactions in powder mixtures [3,5]. Shock-induced chemical reactions are defined as occurring during the shock compression state (i.e. within the shock front). Shock-assisted chemical reactions are those reactions which continue after unloading to ambient pressure. Thus, shock-induced reactions occur within the mechanical equilibrium time scale of several nanoseconds, and shock-assisted reactions are on the thermal equilibrium time scale of a few microseconds. In this investigation no distinction is made between these reactions, as they are indistinguishable in post recovery observations.

Thadhani et al. propose that solid-state diffusionless mechano-chemical processes dominate shock-induced chemical reactions. However, others believe that defect enhanced solid-state diffusionless processes are not possible during the nanosecond duration of the shock state [7-9]. This has led to some controversy as to whether these are solid-solid reactions or solid-liquid reactions. Thadhani asserts that since solid-solid diffusivities of the

powder mixture components are accelerated due to the presence of defects, shorter diffusion distances, and more intimate contacts at high packing densities, liquid-state reactions are inhibited while solid-state reactions are favored under shock compression [3].

There is no question that the high rate of particle deformation (strain rates ~ 10^6 -10^7 s^{-1}) and intimate mixing via intense generation of clean, fresh surfaces significantly increases the reactivity of powders [6-11]. However, it seems unlikely that non-conventional diffusion mechanisms occurring during the microsecond time scale of high pressure shock compression are sufficient to result in the nucleation of new phases. In addition to enhanced diffusional processes, 'non-diffusional' mechano-chemical processes (i.e. atomic rearrangement) are proposed for the ensuing shock-initiated chemical reactions.

3.2 Experimental Procedure

The two powder sizes utilized in this study are a large particle size of -100 mesh Ti and -100 +120 mesh Si (~150 μm), and a smaller particle size with a common mesh size of -325 (~45 μm). The purity level of Ti is 99.5% and that of silicon is 99.9%; The powders are produced by Cerac and Alfa Aesar, respectively. Both powder sizes are mixed in the 5 Ti + 3 Si stoichiometry. The coarse powder is mixed using a portable sieve shaker. Figure 3.1 is a micrograph of the powder morphology. The boxy, shiny single crystals are Si particles and the polycrystalline agglomerates are the Ti particles. A 1,1,2-trifluorethane solution is used to thoroughly mix the fine

powder mixture. The fine powders are dried in vacuum. Figure 3.2 is a micrograph of the fine particle morphology. It is similar to the large particle, the Si are the shiny, boxy particles while the Ti particles are polycrystalline agglomerates.

The powder mixtures are placed into a cylindrical powder cavity and leveled. The powder is then pressed quasi-statically to the desired porosity using a Instron Universal 4204 testing machine. For the porosity range in this study, a load of approximately 9,500 lb. is required. The initial porosity for each experiment is calculated from the measured volume of the powder cavity and mass of the powder used.

The consolidation procedure is performed using the Keck Laboratory Dynamic Compaction Facility. This facility is specifically designed for the consolidation and recovery of powder media. It consists of a 3 meter long by 35 millimeter inner diameter smooth bore barrel in which a propellant driven flyer plate is launched onto a cylindrical powder cavity. A schematic drawing of the facility is illustrated in Figure 3.3. The cylindrical target holder which holds the powder is illustrated in Figure 3.4. The flyer plate is guided down the barrel by a nylon sabot. The target is sealed to the barrel to the left by an assembly which houses the velocity instrumentation and to the right by a momentum trapping assembly. The velocity instrumentation consists of two pairs of fiber optic cables which plug into the barrel extension. The fiber optic cables form a closed loop with one pair of cables serving as light sources and the other pair as receiver cables. Each light source is focused across the

barrel extension onto the receiving fiber optic cable. A tungsten filament lamp is used as the light source. When the first light source is interrupted, it sends a signal to the counter to start and the second light interruption stops the counter. From the total time and the distance between the light sources (4.0 cm), the velocity of the flyer plate can be calculated. This facility is capable of flyer plate velocities of up to 2 km/s.

Before each experiment the barrel is evacuated, back filled with argon and evacuated again to remove any residual oxygen. The barrel is evacuated through a connection to the barrel extension. The final vacuum in the barrel for an experiment is about 0.25 torr. The recovery chamber is also evacuated by a separate vacuum pump for safety and noise control.

The flyer plate strikes only the powder and not the powder confinement. The result of this assembly is a well-controlled plane-wave propagating in the powder [12]. The advantages of the plane-wave geometry is simple characterization of shock conditions, uniform shock conditions across the majority of the material, and the retention of the original shape in two of three dimensions. The powder depth and flyer plate thickness are selected to allow for the initial shock wave traveling in the powder to be unloaded before reaching the solid back. The unloading corresponds to the position at which the shock wave pressure is reduced by the rarefaction wave from the back of the flyer plate. Thus, the powder is subjected to varying shock duration up to the catch-up plane. After this point, the powder is consolidated at a much lower pressure.

A complete summary of the variables for the experiments is listed in Table 3.1, along with calculated parameters. The last column in the Table indicates if the reaction proceeded to completion in the compact. The flyer velocity, initial porosity, and the Hugoniot properties for an unreacted elemental mixture are required to calculate the shock energy and shock pressure for each experiment. The shock parameters for the powder mixture are calculated using a Reuss average and are listed in Table 3.2 [13]. These variables are used in a program which calculates the shock energy, shock pressure, and catch-up distance in the target [12]. These shock parameters can be controlled by the selection of the flyer material, flyer velocity and flyer thickness.

Following the experiment the compacts are removed from the target holder. The compacts which are in the shape of a disk (~32 mm in diameter and 8 mm in depth) are sectioned using a high speed diamond saw. The cross-sections from the compact are mechanically polished and examined optically. X-ray diffraction (XRD) is used to determine if the silicide reaction had been initiated. A Scintag/USA Pad-V diffractometer using Cu Kα radiation (λ = 0.154 nm), with a detection limit of 5% by volume of the element, is used.

3.3 Experimental Results

Visual inspection of the recovered compacts is useful in determining the extent of reaction. In fact, most compacts could be classified under three

categories: fully consolidated with no reaction; partially reacted; and fully reacted. Figures 3.5-3.7 are cross-sections from recovered compacts which fit into the three classifications. Figure 3.5 is a fully consolidated compact with no visible reaction. Figure 3.6 is a reacted compact with shrinkage voids running along the center of the compact. Figure 3.7 is a compact which has undergone complete reaction with a sponge-like texture indicative of rapid solidification of the molten reaction product [2]. The phase diagram for the Ti-Si system is illustrated in Figure 3.8 and Table 3.3 lists thermodynamic properties of the Ti-Si silicides [14,15].

3.3.1 X-ray Analysis

The X-ray diffraction (XRD) data are collected using a Scintag X-ray diffractometer. Figure 3.9 is the XRD data collected for Shot #133 (see Table 3.1) which had no visible signs of reaction; all the diffraction peaks belong to either pure Ti or pure Si with no traces of a silicide. The XRD diffraction pattern for Ti, Si and Ti_5Si_3 are included for comparison. Figures 3.10 is representative XRD data of a reacted compact, along with the diffraction pattern for Ti_5Si_3, Ti and Si for comparison. All the peaks belong to the Ti_5Si_3 silicide, there is no sign of unreacted Si or Ti.

Since the Scintag x-ray diffractometer has a detection limit of approximately 5% by volume, scanning electron microscopy (SEM) is utilized to verify the results obtained from X-ray diffraction. A cross-section from shot #133 which is consolidated just below the threshold shock energy is selected (no observable silicide peaks by XRD). The sample is set in epoxy and

mechanically polished. The sample is polished sequentially with a 6 μm, 3 μm, 1 μm, and 1/4 μm diamond paste.

3.3.2 SEM Analysis

The silicide reaction that is undetected from XRD analysis is clearly visible by SEM. Figure 3.11 is the backscattered SEM micrograph of the compact from shot #133. The grayish areas are reaction spots; a few of them are labeled. The dark particles are Si and the light regions are Ti. Reaction occurs at the Si/Ti interface and is seen throughout the cross section in isolated regions. From Energy Dispersive Spectroscopy (EDS), the composition of the reaction product had a stoichiometric ratio of Ti to Si corresponding to the $TiSi_2$ silicide. Since $TiSi_2$ has the lowest melting temperature (1843 K) of all the titanium silicides, it is very likely that it will form first. The melting temperature and the heat of formation for the Ti-Si silicides are listed in Table 3.3 [14].

Figure 3.12 is a backscattered SEM micrograph at a significantly higher magnification and indicates the presence of a molten reaction product. The swirl-like structures within the circular-shaped region in the middle of the micrograph are indicative of convective flow, which greatly enhances the heat transfer from the reaction to the cooler areas [16]. Extensive EDS analysis of the entire region including the dark and light bands within the circular region is performed. The composition of the entire region is that of $TiSi_2$.

3.3.3 Reaction Growth Mechanism

The growth mechanism by which the reaction propagates is evident in Figure 3.13. The darkest region is Si, the lightest area in the upper right-hand corner is Ti, and the grayish region with swirl-like structures in the center is reaction product. Spherical nodules appear to form at the interface between the solid titanium and liquid silicon. Meyers et al. have propose a critical melt size of Si which corresponds to the threshold shock energy [8,9].

Meyers et al. propose that the metal-Si interface grows from the dissolution of the metal into molten Si, producing the molten intermetallic, followed by spherodization, solidification, and expulsion into surrounding liquid silicon melt. The detachment of the spherules from the interface may be assisted by the turbulent flow of the silicon melt. A schematic of the process is illustrated for the formation of Nb silicide in Figure 3.14 . The sequence of events is as follows: initially, the nucleation and growth of a thin layer of the reaction product occur at the *solid* Nb - *Liquid* Si interface under shock loading (Fig. 3.14 a, b and c); the spherodization of the reaction product occurs as interfacial forces become dominant (Fig. 3.14 d); the onset of solidification of the newly formed spheroid leads to the formation of additional reaction product at the neighboring regions of newly exposed surface (Fig. 3.14 e & f); as the adjacent regions start to solidify they start exerting forces, and the first spherule is ejected into the molten Si (Fig. 3.14 g and h). This process continues undisturbed until all of the reactants are consumed.

3.3.4 Shock Energy Analysis

The shock energy and equilibrium temperature as a function of the powder porosity are plotted in Figure 3.15. The circles and diamonds represent the small and large powder mixtures, respectively. The filled circles and diamond represent those experiments where the reaction proceeded to completion. The equilibrium temperatures listed on the plot are valid for only those shots with no reaction, since the equilibrium temperature is calculated assuming no reaction and adiabatic conditions. In a powder medium the homogeneous temperature rise can be approximated by (assuming all the shock energy is converted into heat) [10]:

$$\int_{T_o}^{T_h} C_p dT = E_s \tag{3.2}$$

C_p is the specific heat (J/g/^oC) which is a function of temperature and pressure, T_o is the initial powder temperature, and T_h is the homogeneous temperature. In our pressure range the effects of pressure on the specific heat are insignificant, and hence only the temperature dependence is considered. The expression for the specific heat as a function of temperature is obtained by curve-fitting experimental data [17] :

$$C_p = a + 10^{-3}\, bT + 10^{-5}\, cT^{-2} \tag{3.3}$$

where a, b and c are known constant for each element. These constants for Ti and Si are listed in Table 3.2. For a given shock energy, the homogenous

temperature is obtained by solving the above equation with the corresponding weighted integral for each of the elements.

3.3.5 Powder Size Effect

The threshold shock energy is substantially higher for the large particle powder mixture (see Figure 3.15). This increase in threshold shock energy is primarily attributed to the increase in area in the interior of each particle, which acts as a heat sink. For the large particles there is an increase in the ratio of specific volume to surface area. During dynamic consolidation, the energy is preferentially deposited on the particle surface by frictional sliding and plastic deformation leaving the interior of the particle relatively cool [19,20]. Thus, the increase in area in the interior of the particle which serves as a heat sink greatly enhances the cooling rate of the reaction. A secondary reason for the increase in threshold shock energy for the large particle mixture is the decrease in surface area of reactants in contact.

3.3.6 Initial Porosity Effects

There is an increase in the threshold shock energy as the initial porosity of the powder is decreased for both of the powder mixtures. As the porosity is decreased from 49% to 41%, there is an approximate increase in the threshold shock energy of 75% (see Figure 3.15). This increase is observed for both powder sizes. The increase in threshold shock energy is due to the reduction in shear deformation for the powders with lower initial porosity. Meyers et al. demonstrated that intense localized shear deformation can trigger the exothermic reaction between niobium and molybdenum

disilicides at shock compression pressures below the threshold value for shock-induced reactions. They propose that the plastic deformation provides the added driving energy for the reaction [8,9,21].

The formation of hot spots as a result of void collapse is modeled by Taylor et al. [22]. The heat conduction model employs the conservation of mass and the law of mass action. They conclude that these hot spots lead to enhanced chemical reactivity. A study by Tong and Ravichandran finds that dynamic effects from pore collapse can be significant under shock wave consolidation conditions. The distance available for frictional sliding is greatly reduced for closely packed powders (i.e., low porosity) resulting in a reduction of frictional heating [23].

3.4 Reaction Rate Analysis

The Ti_5Si_3 reaction is extremely exothermic, for this reason it is a popular candidate for combustion synthesis, also known as self-propagating high-temperature synthesis (SHS) [14,24-27]. The microstructure of the recovered compacts after shock synthesis are similar to those produced by combustion synthesis. Following SHS, most materials are riddled with shrinkage voids and cracks [24]. It is important to study the reaction rate in order to improve the final microstructure of the silicide.

The rate of reaction for the formation of Ti_5Si_3 from the elemental powder mixture with the same stoichiometric composition is estimated by Chen et al. in their study of shear-induced chemical reactions [21]. Their

analysis is based on an area of unreacted material which had undergone localized high-strain-rate shear deformation. They infer that the reaction rate within the area must have been lower than the rate of heat loss within the region. Figure 3.16 is a schematic representation of the triangular region modeled. The reaction propagates within the specimen except in this triangular region, as a result of a displacement discontinuity due to shear localization [21,28]. The area is bounded by Ti_5Si_3 reaction on one side and a copper confinement on the other.

Assuming negligible heat losses to the surroundings and constant thermophysical properties, the calculations are fairly straightforward. The computation begins with the conservation of energy equation for a propagating planar 'gasless' combustion wave traveling in an homogeneous, isotropic material [27,29]:

$$\frac{\partial T}{\partial t} = \alpha \frac{\partial^2 T}{dx^2} + \frac{Q}{C_p}\frac{\partial \eta}{\partial t} < 0 \tag{3.4}$$

where,

$$Q\frac{\partial n}{\partial t} = \dot{Q}_r \tag{3.5}$$

is the rate of heat release of the reaction, and

$$\frac{\partial \eta}{\partial t} = K_o(1-\eta)^N Exp\left[\frac{-E}{RT}\right] \tag{3.6}$$

is the reaction rate. α is the thermal diffusivity; Q is the heat of reaction; η is the degree of conversion; N is the order of reaction; K_o is the reaction-rate constant; E is the activation energy; and R is the universal gas constant. The maximum cooling rate for this reaction under similar conditions is estimated in a previous study to be $Q_{loss}=4.5 \times 10^5$ J/g·s [29,20]. Thus, the heat release

rate of the reaction must be less than this maximum cooling rate in order to quench the reaction. The maximum heat release rate will occur at the adiabatic temperature (T_{ad} =2403 K for 5Ti + 3Si --> Ti_5Si_3); it is assumed that adiabatic conditions hold for these reactions. From the conservation of energy equation, solving for the heat release rate yields;

$$\dot{Q}_r < -\alpha C_p \frac{\partial^2 T}{\partial x^2} \tag{3.7}$$

Their calculations show a reaction rate (at T_{ad}) of $\frac{\partial \eta}{\partial t} = 250 s^{-1}$.

Since the reaction rate has an exponential dependence on temperature, it must be solved for different temperatures. To obtain the reaction rate at different temperatures, Chen et al. further assume that this is a first-order (N=1) reaction which yields a constant reaction-rate constant (K_o). The results are plotted in Figure 3.17, for a 50%, 55% and 60% conversion, η.

Our experimental observations differ since we do not produce shear bands in our specimen. However, the reaction rate should be the same for the same system under comparable strain rates and temperatures. We see isolated regions of reaction product with a stoichiometric composition of $TiSi_2$ as identified from EDS analysis. The $TiSi_2$ disilicide reaction appears to be initiated first, followed by an intense exothermic reaction to Ti_5Si_3 when the temperature within the reaction zone reaches a critical temperature.

A model is proposed to determine the initial rate for the disilicide ($TiSi_2$) formation. This model is consistent with the reaction mechanism

proposed by Meyers et al. (Figure 3.14) [8,9]. The critical rate is defined as the minimum reaction rate needed to sustain the reaction in order to balance the heat loss to the surrounding with the heat generated by the formation of the silicide. Our calculations hold only for the initial rate since the rate will be temperature dependent. The critical reaction rate will result in a temperature increase at the Ti-Si interface for a given shock energy.

There exists a multitude of possible parameters that could affect the initiation of the shock reaction process. The parameters include the powder material characteristics (yield strength, mechanical impedance, isentropic compressibility), compatibility of powder mixtures (diffusivity of one species into the other, equilibrium reaction product), powder morphology (spherical, irregular, etc.), initial porosity, initial conditions (pressure, temperature), inert or air atmosphere, and exothermic reaction. However, this model in no way attempts to address all these issues. This is only a qualitative analysis of the initial reaction rate for the disilicide reaction.

It is not practical to model the random arrangement of silicon and titanium particles. The powder's macroscopic arrangement is modeled as a periodic composite slab of solid silicon, molten silicon, and solid titanium. Figure 3.18a is the macroscopic microstructure with randomly dispersed Si particles in a Ti matrix. The random Si particles with interparticle melting are modeled periodically (Figure 3.18b). This periodic sequence can be further simplified to a single composite slab (Figure 3.18c). This periodicity is consistent with experimental observations [7-9]. The preferential deposition

of shock-wave energy on the particle surface results in melting at the interface of the Si and Ti particles [1-5,8-11]. The silicon melt pool serves as the initiation site for the silicide reaction [9] (Figure 3.18d). Depending on the shock energy and rate of reaction, either the melting will be followed by rapid solidification via heat conduction into the interior of the particles or, the reaction will proceed as in self-propagating high-temperature synthesis.

Since the model only addresses the disilicide formation for very short times, it is incorporated as a heat source at the molten silicon - solid titanium interface. The thermodynamic properties of the interface are assumed to be those of silicon since the amount of reaction product is small in comparison to the molten silicon. Figure 3.18 is a schematic representation of succession of steps leading to the 1-D model. The following assumptions are made:

(1) The thermophysical properties remain constant within each layer.

(2) $\frac{\partial T(x,t)}{\partial x} = 0$ at $x = d, -d$ (d is the half the particle diameter).

(3) $T(x,0) = 300$ K for $x<-\delta$ and $x>0$

The Si melt thickness considered is 1/8 of the initial particle diameter. This fraction is consistent with theory and experimental observations [7,20]. Schwartz et al. derived the following expression for the temperature rise of the unmelted portion of the particles (i.e., the interior of the particle) after the initial shock wave by considering the solid to be shocked to a pressure P along the Rayleigh line between state 0 and 1:

$$T' = T_o + \frac{1}{C_p}\left[P(V_o - V_1)/2 - \int_{V_1}^{V_o} PdV \right] \tag{3.8}$$

T′ is the temperature in the interior of the particle; T_o is the initial temperature of the powder; and V is the specific volume. For the pressure range in this study, $T' \approx T_o$ (room temperature).

The governing equation is the heat conduction equation:

$$\rho(x)C_p(x)\frac{\partial T}{\partial t} = \frac{\partial}{\partial x}\left[k(x)\frac{\partial T}{\partial x} \right] + q(x) \tag{3.9}$$

$$q(x) = h_f \dot{r} \tag{3.10}$$

ρ is the density , Cp is the heat capacity , k is the thermal conductivity and q is the heat of reaction {heat of formation (h_f) multiplied by the reaction rate ($\dot{r}$)}.

This partial differential equation is discretized in space via a finite element formulation (with a weak form of the equation) which leads to the semidiscrete system of ordinary differential equation's [ODE] where {T} is the vector of nodal temperatures and $\{\dot{T}\}$ its time rate [32].

$$[C]\{\dot{T}\} + [K]\{T\} = \{q\} \tag{3.11}$$

This system of ODE's is solved in time using the Forward Euler method

(explicit algorithm) starting from the initial conditions given below.

$$(1)\ \frac{\partial T(x,t)}{\partial x} = 0 \quad \text{at} \quad x = d, -d, \text{ for all t}$$

(2) $T(x,0) = 300$ K for $x<-\delta$ and $x>0$

(3) $T(x,0) = 1685$ K for $-\delta \le x \le 0$

The first condition corresponds to zero heat flux at the boundary of the particle. The second and third conditions yield a step profile for the initial temperature (i.e., the solid layers are at room temperature and the molten layer is at the melting temperature of Si). The values for the thermal conductivity and specific heat are listed in Table 3.4. A short fortran program is written to solve the system of ODE's and is included in the Appendix.

The objective of the analysis is to determine the initial reaction rate necessary to produce enough heat to propagate the reaction (i.e., retain some fraction of molten silicon). This minimum reaction rate must be sufficiently high so as to balance the heat conduction away from the molten Si - solid Ti interface to the particle interior. Since the model is valid only for the initial rate, the reaction time is limited to 10 ns. This is a fraction of the expected rise time of the shock (~75 ns).

For a melt fraction of at least 1/8 of the solid particle the minimum reaction rate is estimated to be approximately 400 s^{-1}. This is the minimum reaction rate needed to sustain the reaction. Figure 3.19 is a plot of the reaction rate analysis for the initial conditions listed above and reaction rates of 350 s^{-1}, 400 s^{-1}, 450 s^{-1}, and 500 s^{-1}. These curves represent a total reaction

time of 9 ns. The kink in the temperature profile at the solid Si - molten Si interface corresponds to the change in thermophysical properties between them.

3.5 Discussion

The equilibrium temperatures calculated for the unreacted powders are well below the melting temperature of both Si and Ti, yet isolated regions of melting leading to the silicide formation are observed. The silicon melts first since it has a lower melting point which is known to decrease by as much as 54 ^{o}K/GPa [14]. This results in a significant decrease in temperature for the large particle powder mixture where the shock pressure is as high as 7.28 GPa.

The isolated molten regions are believed to be a result of higher than average initial porosity in these regions. These areas of high porosity act as hot spots in the initiation of the silicide reaction [9]. The higher than average porosity areas assist the silicide reaction in two ways: increases shear and plastic deformation, thus increasing the temperature from conversion of plastic work to heat; and, provides sites for molten reaction product to flow into and mix. Hence, the mixing efficiency is greatly improved for areas with higher porosity. This is consistent with the CONMAH model, where good mixing of the constituents is a crucial step of the reaction initiation [11].

The role of shear and plastic deformation in reaction initiation are studied extensively by Meyers et al. [16,18,21,30]. They demonstrate that intense localized shear deformation can trigger the exothermic reaction

between Nb and Si particles, and Mo and Si particles at shock energies below the threshold value for shock-induced reaction. Yu and Meyers conclude that the plastic deformation provides the added driving energy for reaction initiation [26]. In fact, they propose the addition of this plastic deformation energy to the total energy (i.e., conservation of energy equation).

Below the threshold energy level, localized reaction zones are quickly quenched by the cooler particle interiors and surrounding particles. Above the threshold shock energy, the reaction cannot be quenched quickly enough and the reaction proceeds to completion. The two conditions for self-sustained exothermic mixing reaction to occur, proposed by Bordeaux and Yavari, can be examined [6]. The first condition is that the heat released must be well in excess of the heat of fusion needed to melt the sample. The second requires the mixing reaction time to be much shorter than the time required for the dissipation of the heat to the environment.

The first condition can be verified from calculations for combustion and shock synthesis of silicides under adiabatic conditions [14,22]. For the Ti_5Si_3 self-propagating reaction to occur, the enthalpy of reaction must be supplied by the negative enthalpy of the formation of the silicide plus the threshold shock energy. For this study, the threshold shock energy values reported for the reacted samples are sufficient to heat and melt the silicides [6].

The second condition that requires the mixing reaction time to be much shorter than the time for dissipation of heat to the surroundings (i.e.

particle interior, target holder and flyer plate), assuming adiabatic conditions, needs further assessment. This condition is difficult to verify since the size or shape of the molten zone where the reaction is initiated is not known. The molten areas where turbulent mixing is present would likely satisfy this condition since the mixing efficiency is optimal in these areas. From a structural point of view, this condition reduces to the requirement of very short diffusional distances to allow for short mixing times. These short diffusional distances are common during the shock consolidation process as documented in the ROLLER model discussed in chapter 1 [31].

The silicide formation may also be assisted by the negative pressure-temperature dependence of silicides; The melting temperature decreases with increasing pressure for silicides. The melting temperature of Si decreases by 54 K/GPa.

3.6 Conclusions

The threshold shock energy for reaction in the large powder mixture is much greater than that of the small powder mixture. The larger particles have an increased volume per unit area which acts as a heat sink to quench the reaction. There is also a decrease in the specific area of reactant in contact for the larger particles.

As the initial porosity is decreased the threshold shock energy for reaction increases for both powder mixtures. The voids which serve as initiation sites for the reaction are significantly reduced as the porosity

decreases. In addition, the amount of shear deformation, a critical factor in reaction initiation, decreases with decreasing porosity.

Reaction initiation occurs at the molten Si - solid Ti interface. The reaction appears to proceed by the formation of spherules at the interface which are ejected into the molten silicon. The first reaction product to form is identified as $TiSi_2$ from the stoichiometric ratio of Ti and Si which subsequently reacts with Ti to form Ti_5Si_3 in a vigorous exothermic reaction. Under adiabatic conditions, Ti + 2Si reacts with a resulting temperature which melts the $TiSi_2$. There is an excess of Ti after complete reaction of the Si to $TiSi_2$. The molten Ti and $TiSi_2$ react to form Ti_5Si_3:

$$Ti + 2\,Si \text{ ----> } TiSi_2 - 133.54\ KJ/mol$$

$$7\,Ti + 3\,TiSi_2 \text{-----> } 2\,Ti_5Si_3 - 138.4\ KJ/mol$$

The initial reaction rate for the disilicide reaction for an initial melt zone equal to 1/8 of the initial particle diameter is approximately 400 s^{-1}. Figure 3.19 are the results of the analysis for reaction rates equal to 350 s^{-1}, 400 s^{-1}, 450 s^{-1}, and 500 s^{-1} along with the initial step profile. The curves represent a total reaction time of 9 ns. At a rate of 350 s^{-1} the temperature at the interface drops below the melting temperature of Si, while a rate of 400 s^{-1} is just sufficient to maintain the melting temperature at the interface.

Table 3.1 Experimental data for shots performed

Shot #	Powder Size	Porosity	Impact Velocity (m/s)	Shock Energy (J/g)	Shock Temp. (°C)	Shock Press. (GPa)	Catch-up Distance (mm)	Go / No Go
99	S	0.429	757	237	401	2.29	2.95	no
100	S	0.46	693	206	355	1.75	2.34	no
101	S	0.482	650	185	323	1.44	1.97	no
104	S	0.487	965	386	615	2.94	3.13	go
105	S	0.487	915	350	564	2.67	2.93	go
111	S	0.487	717	223	380	2.91	2.17	no
112	S	0.444	972	378	604	3.42	3.76	go
113	S	0.444	837	293	483	2.61	3.13	go
116	S	0.492	487	108	203	0.8	1.34	no
121	S	0.487	773	256	429	1.97	2.4	go
122	S	0.415	829	275	457	2.85	3.54	no
123	S	0.487	693	209	359	1.59	2.08	go
135	S	0.406	969	310	507	3.83	4.4	go
136	S	0.434	775	248	417	2.3	2.96	no
139	S	0.443	804	267	445	2.42	2.98	no
124	L	0.487	740	236	399	1.8	2.56	no
125	L	0.487	783	262	437	2	2.42	no
126	L	0.487	855	308	504	2.35	2.69	no
133	L	0.49	917	351	566	2.65	2.91	no
134	L	0.487	966	385	614	2.94	3.13	go
198	L	0.444	1050	432	675	3.92	4.14	no
199	L	0.444	1070	447	695	4.05	4.23	no
200	L	0.432	1215	552	845	5.27	5.22	go
201	L	0.4012	1391	671	994	7.28	7	go

$S \leq 45\ \mu m$: $L \leq 150\ \mu m$

3.2 Shock parameters for Ti, Si and 5 Ti + 3 Si mixture

Shock parameter	Ti	Si	5Ti + 3Si
Volume fraction	0.594	0.406	1.0
Initial Density (g/cm^3)	4.52	2.33	3.631
Adiabatic bulk[b] modulus (GPa)	108	97.88	103.71
Isentropic[b] Compressibility (GPa^{-1})	0.00926	0.0122	0.00965
Gruneisen[b] coefficient	1.13	0.4	0.649
Shock Coefficient[a] (Km/s/GPa)	0.95	1.3	1.066
Shock Velocity[a] (Km/s) [at P=0]	4.94	6.5	5.342
Specific Heat Constants[c] a b c	5.28 2.4 0	5.72 0.59 -0.99	–

[a] LASL Shock Hugoniot Data

[b] Smithell's Metals Handbook

[c] CRC Materials Science and Engineering Handbook

Table 3.3 Thermodynamic properties of Ti, Si and Silicides

	Melting point[a] (K)	Heat of formation[a] ΔH_f at 298 K (KJ/mol)	Heat of fusion[a] ΔH_m (KJ/mol)
Ti	1933	-	20.92[b]
Si	1685	-	39.62[b]
TiSi	1843	-128.96	40.18
$TiSi_2$	1773	-133.54	43.44
Ti_5Si_3	2408	-138.4	178.88

[a] Bhaduri, Qian, and Radhakrishnan, Scr. Metall. Mater. 30, 179 (1994)

[b] CRC Materials Science and Engineering Handbook, CRC Press (1992)

Table 3.4 Thermophysical properties of Ti and Si

Property	Density, ρ (g/cm^3)	Thermal Conductivity[a] K (J/s/cm/K)	Specific Heat[b], C_p (J/g/K)
Ti	4.51	0.197	0.6775
Si	2.33	0.508	0.8636
Si at T_m	2.33	0.8636	1.037

[a] Thermophysical Properties of Matter. v1: Thermal Conductivity - Metallic elements and alloys, ed. by Y.S. Toulaukian. New York-Washington, IFI/Plenum, p. 326 (1970).

[b] Thermophysical Properties of Matter. v4: Specific Heat- Metallic elements and alloys, ed. by Y.S. Toulaukian. New York-Washington, IFI/Plenum, p. 204 (1970).

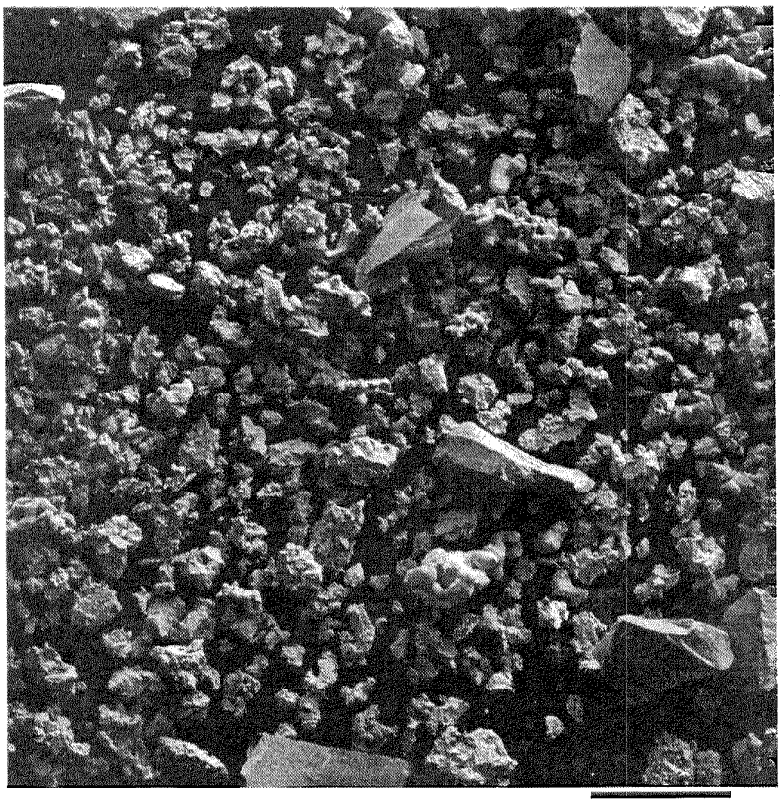

Figure 3.1 Backscattered SEM micrograph of large 5Ti+3Si. Large boxy particles are Si and the agglomerates are Ti.

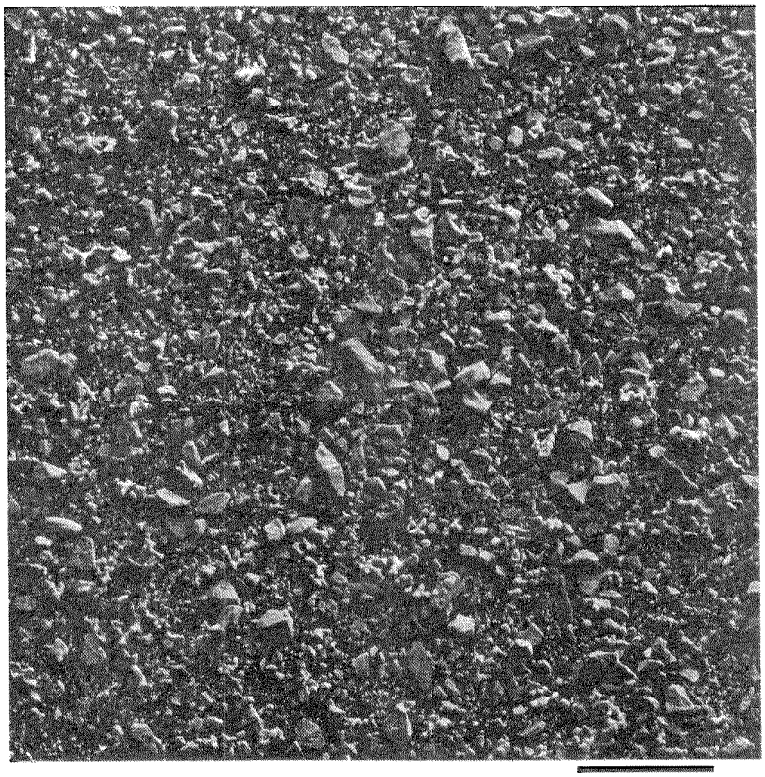

Figure 3.2 Backscattered SEM micrograph of small 5Ti+3Si. Large boxy particles are Si and the agglomerates are Ti.

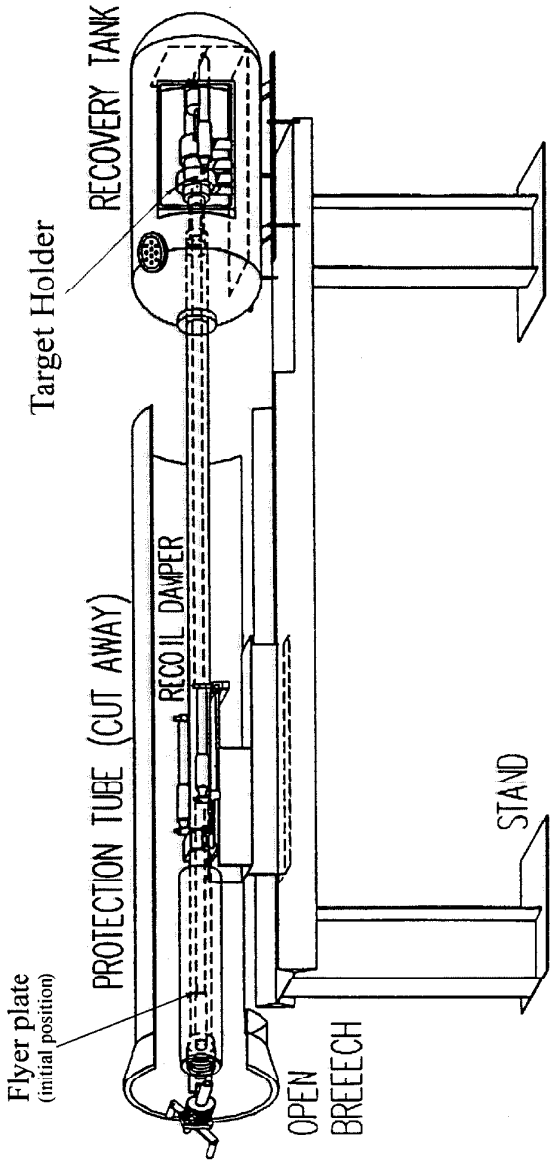

Figure 3.3 Scale drawing of Keck Laboratory Shock Compaction Facility.

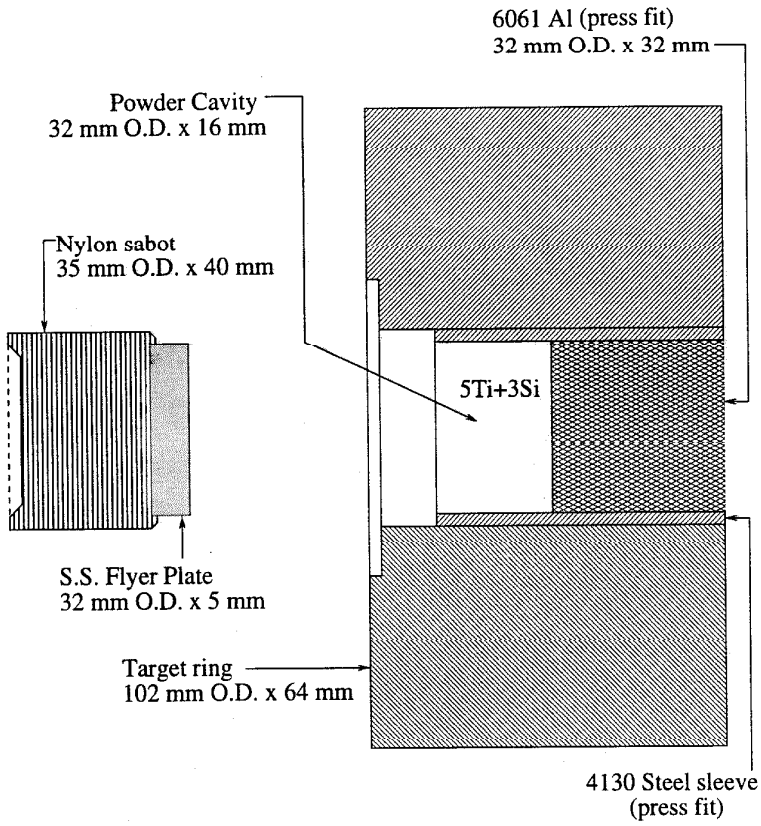

Figure 3.4 Schematic drawing of the sabot with flyer plate and target design.

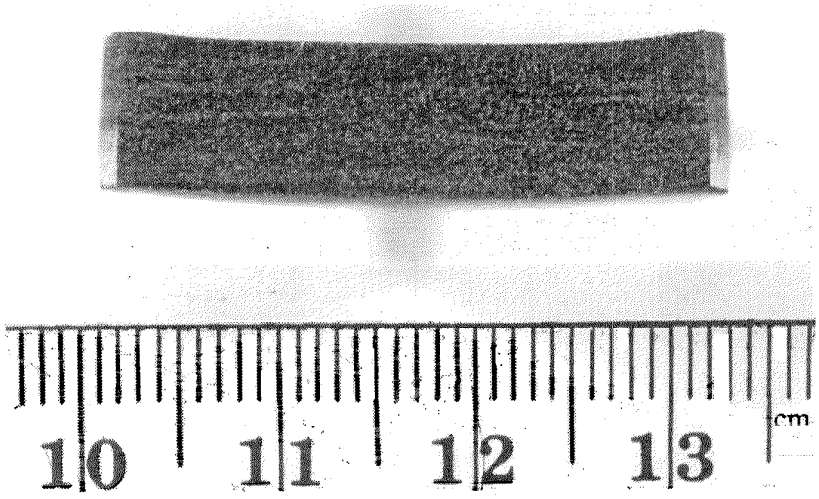

Figure 3.5 Cross-section of unreacted compact (Shot #182).

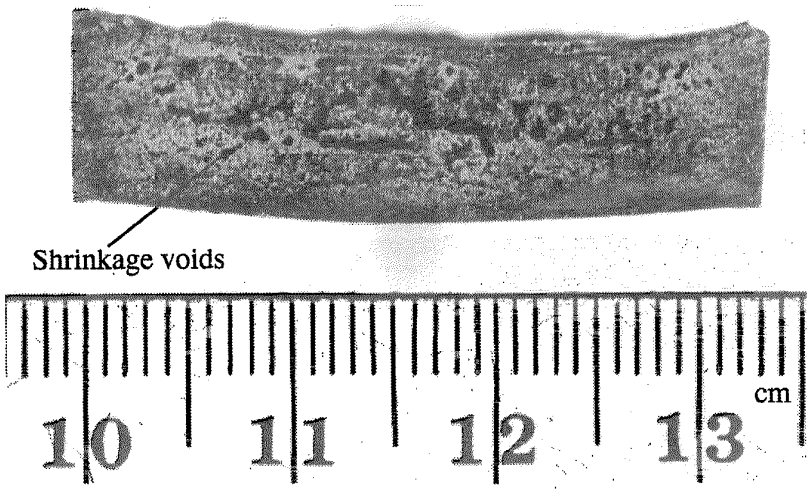

Figure 3.6 Cross-section of partially reacted compact (Shot #201)

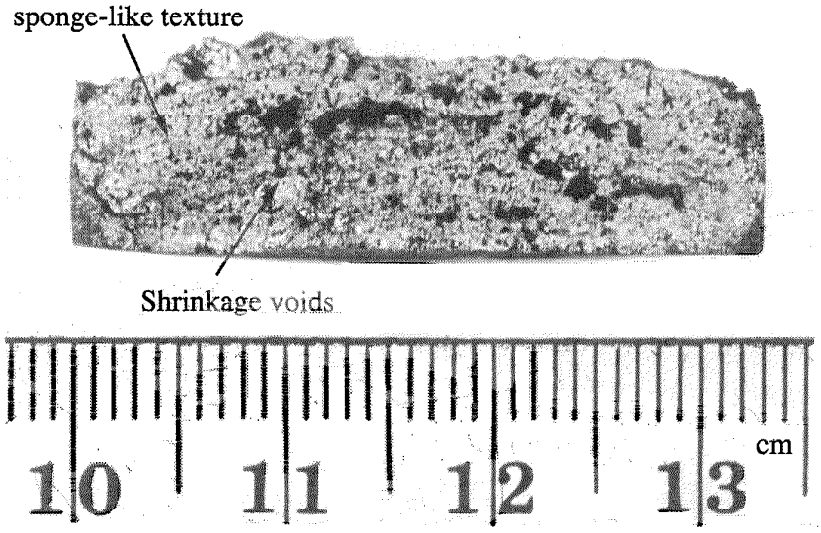

Figure 3.7 Cross-section of fully reacted compact (Shot #189).

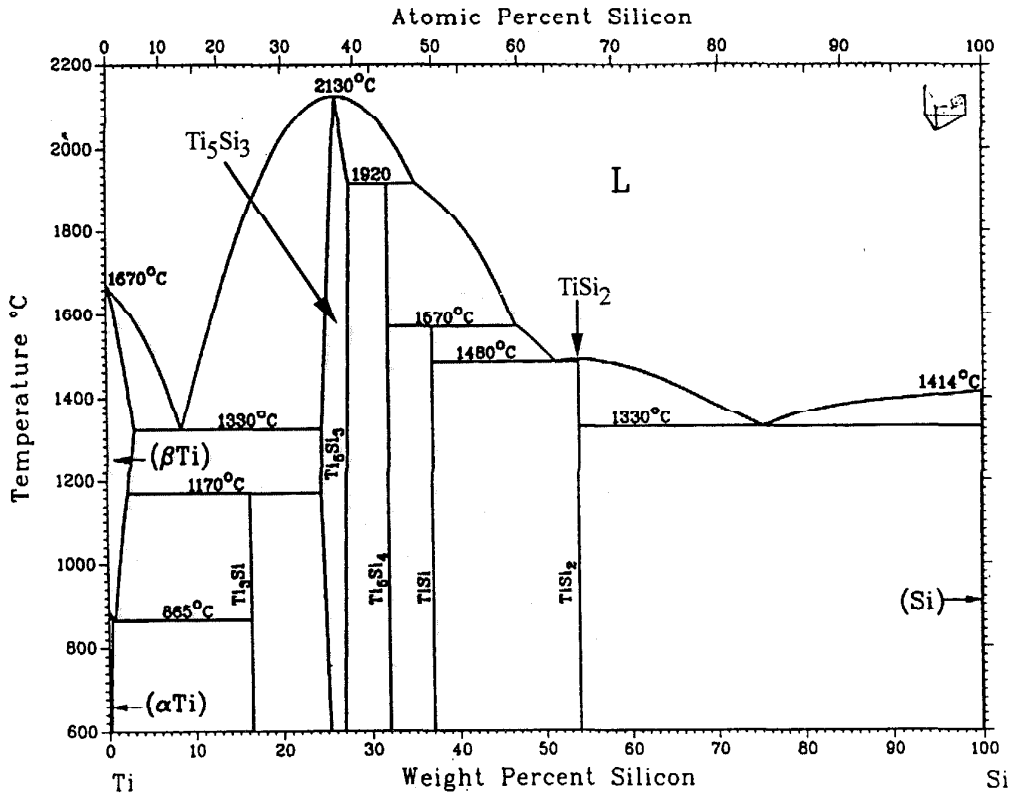

Figure 3.8 Binary phase diagram for Ti-Si system [15].

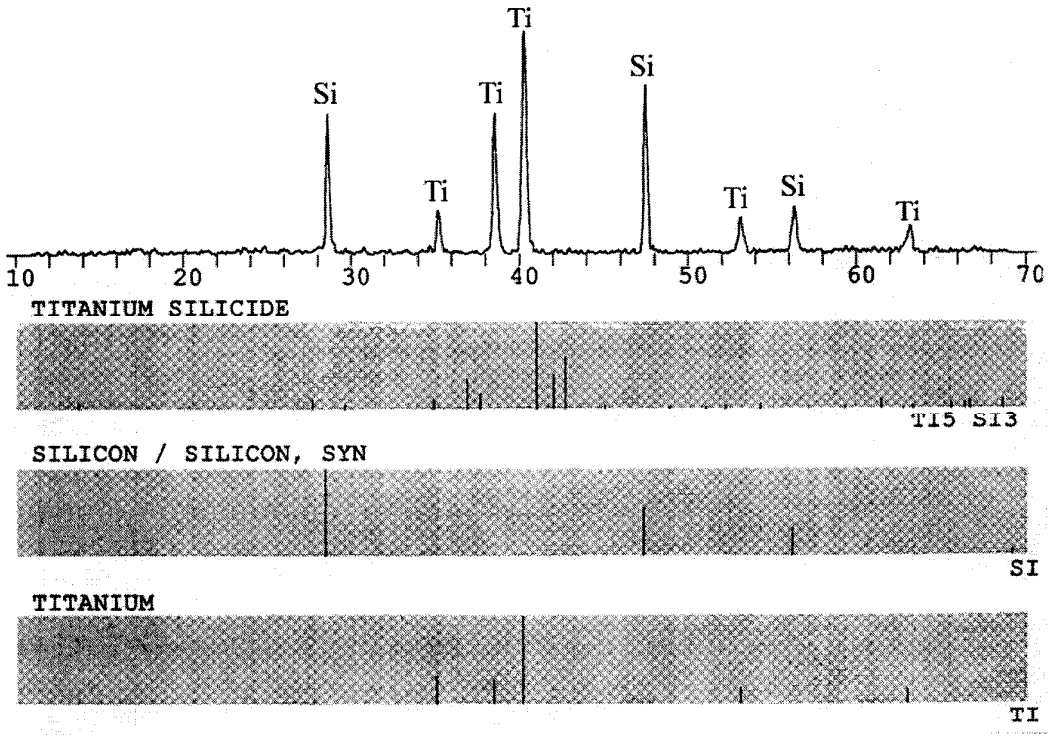

Figure 3.9 X-ray diffraction data for unreacted compact (Shot #133).

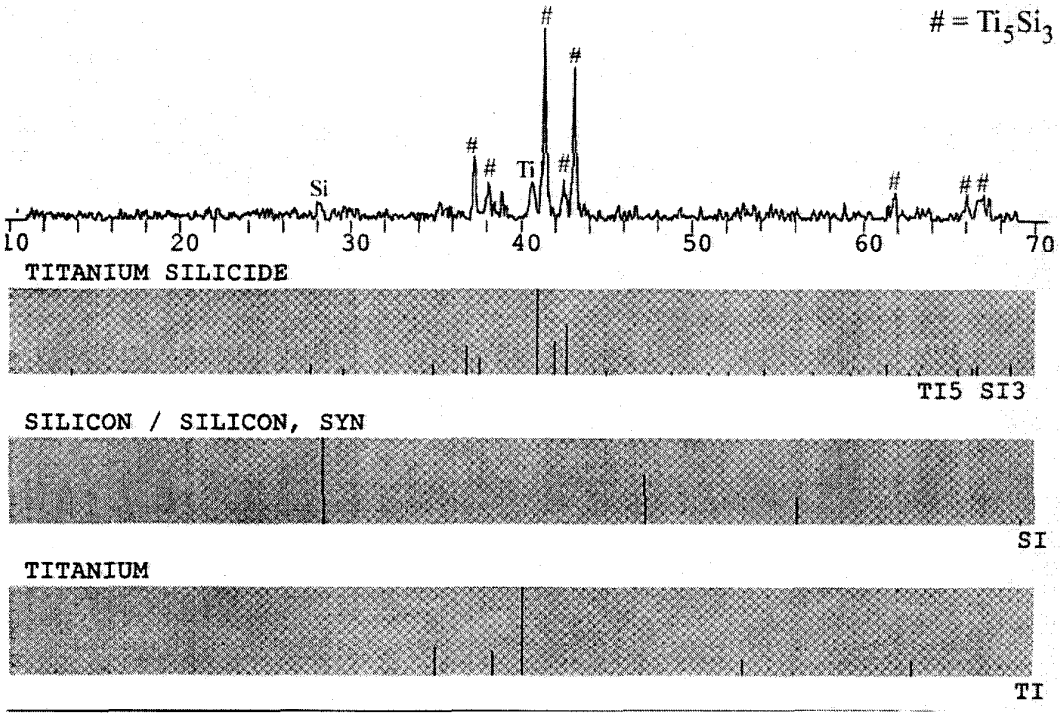

Figure 3.10 X-ray diffraction data for reacted compact (Shot #210).

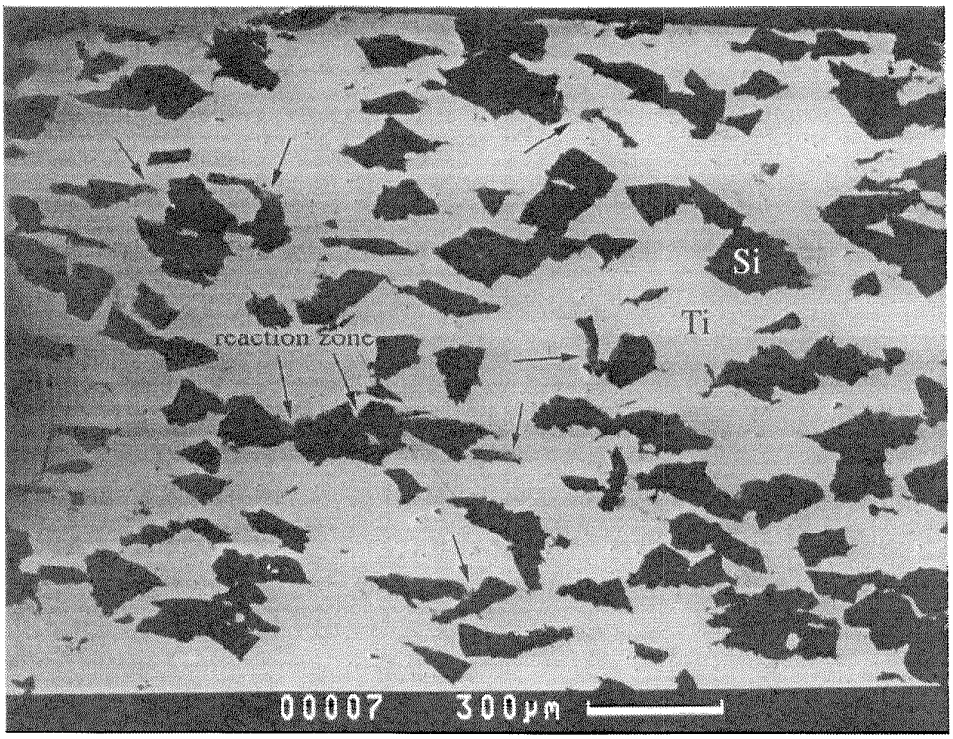

Figure 3.11 Backscattered SEM micrograph of isolated reaction areas (Shot #133).

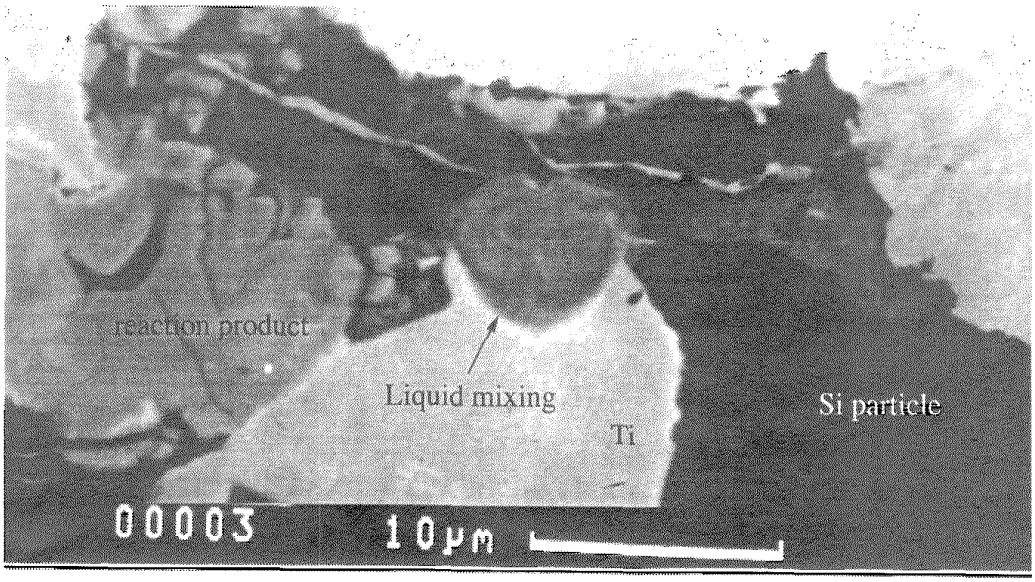

Figure 3.12 Molten reaction zone with liquid mixing (Shot #133).
Dark particles are Si and light matrix is Ti.

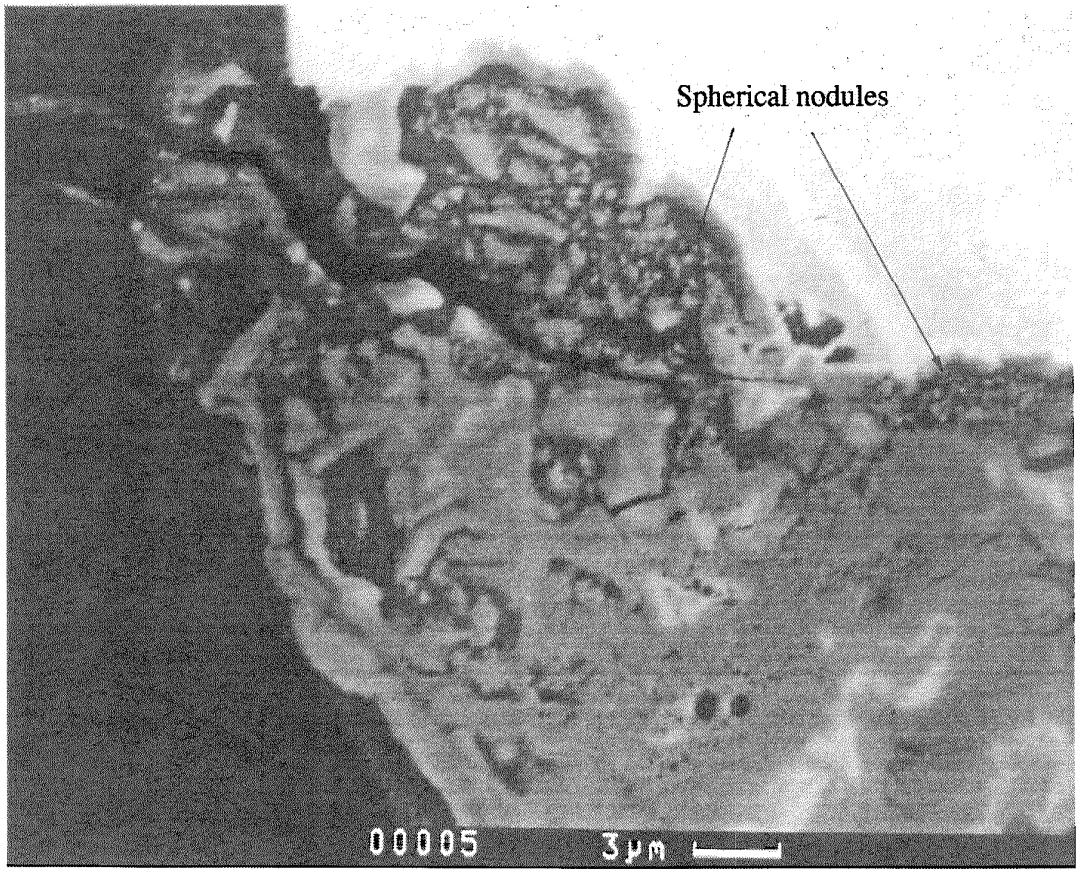

Figure 3.13 Reaction growth mechanism in progress (Shot #133).

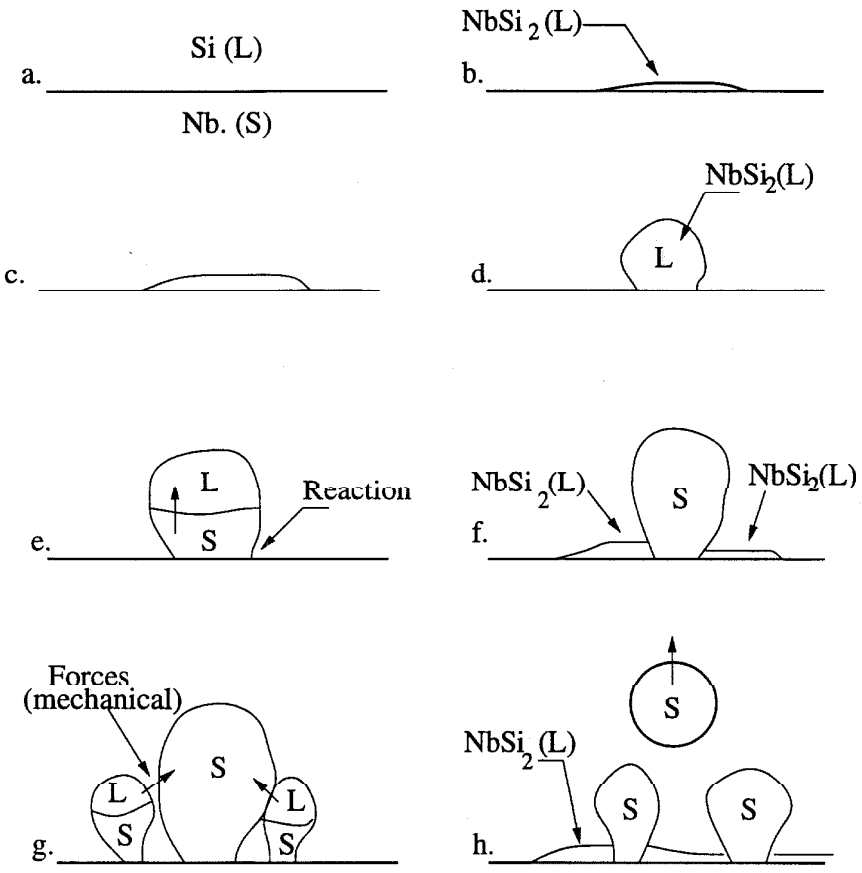

Figure 3.14 Reaction growth mechanism proposed by Meyers et al. [9].

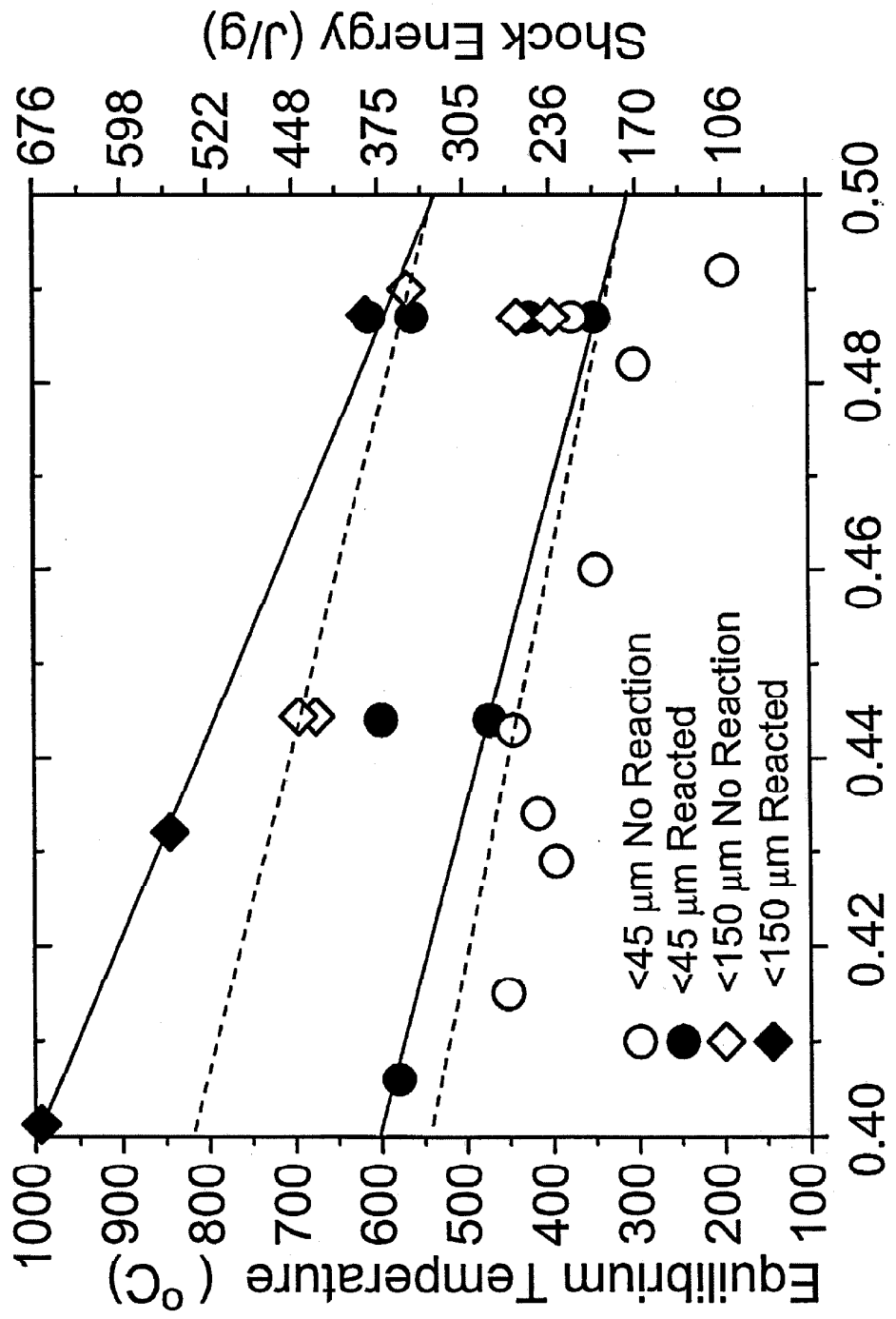

Figure 3.15 Shock energy vs initial porosity of experimental shots.

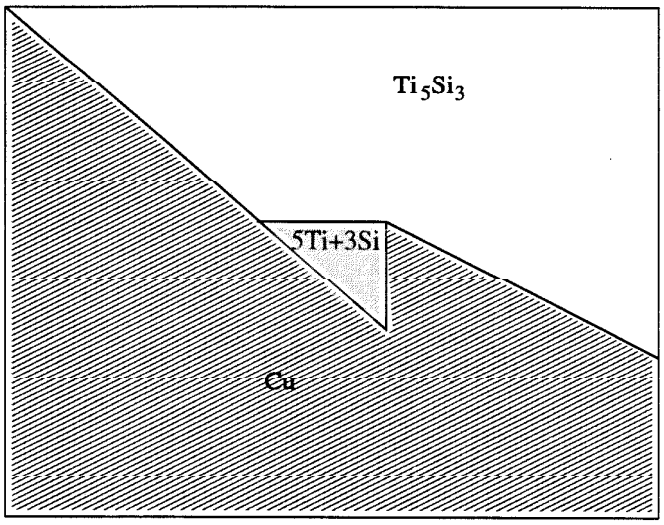

Figure 3.16 Schematic representation of triangular region [21].

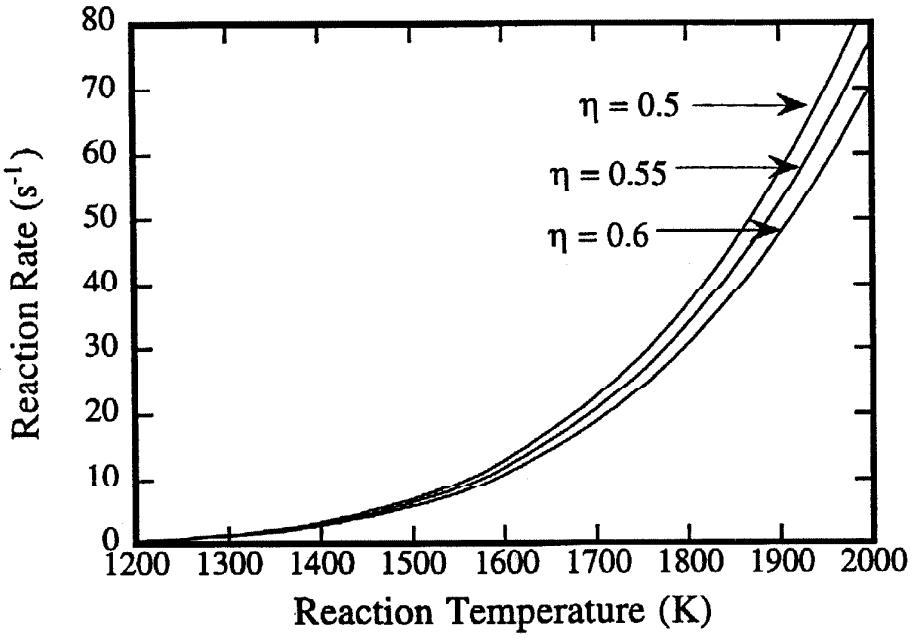

Figure 3.17 Reaction rate vs temperature of 5Ti + 3Si system due to shear deformation (η is degree of convergence)[21].

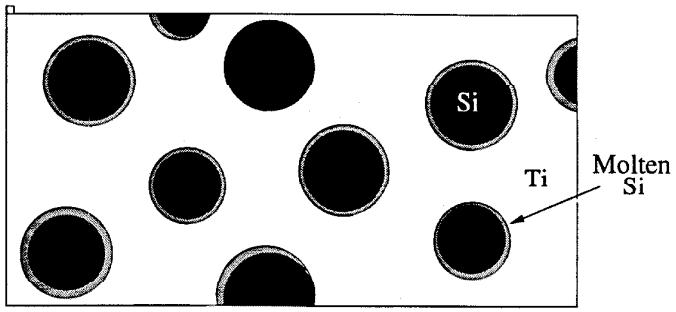

a. Schematic representation of cross-section

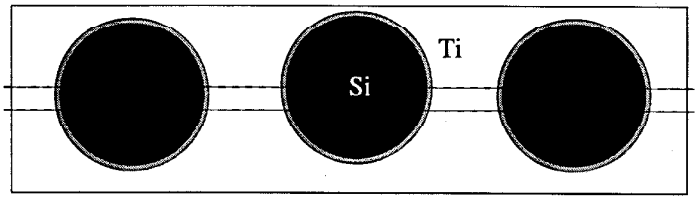

b. Periodic arrangement with interparticle melting

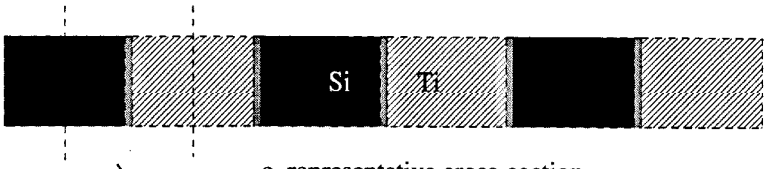

c. representative cross-section

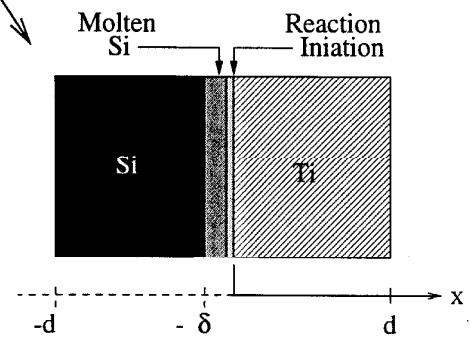

d. Model representation with reaction initiation

Figure 3.18 Schematic of reaction rate model

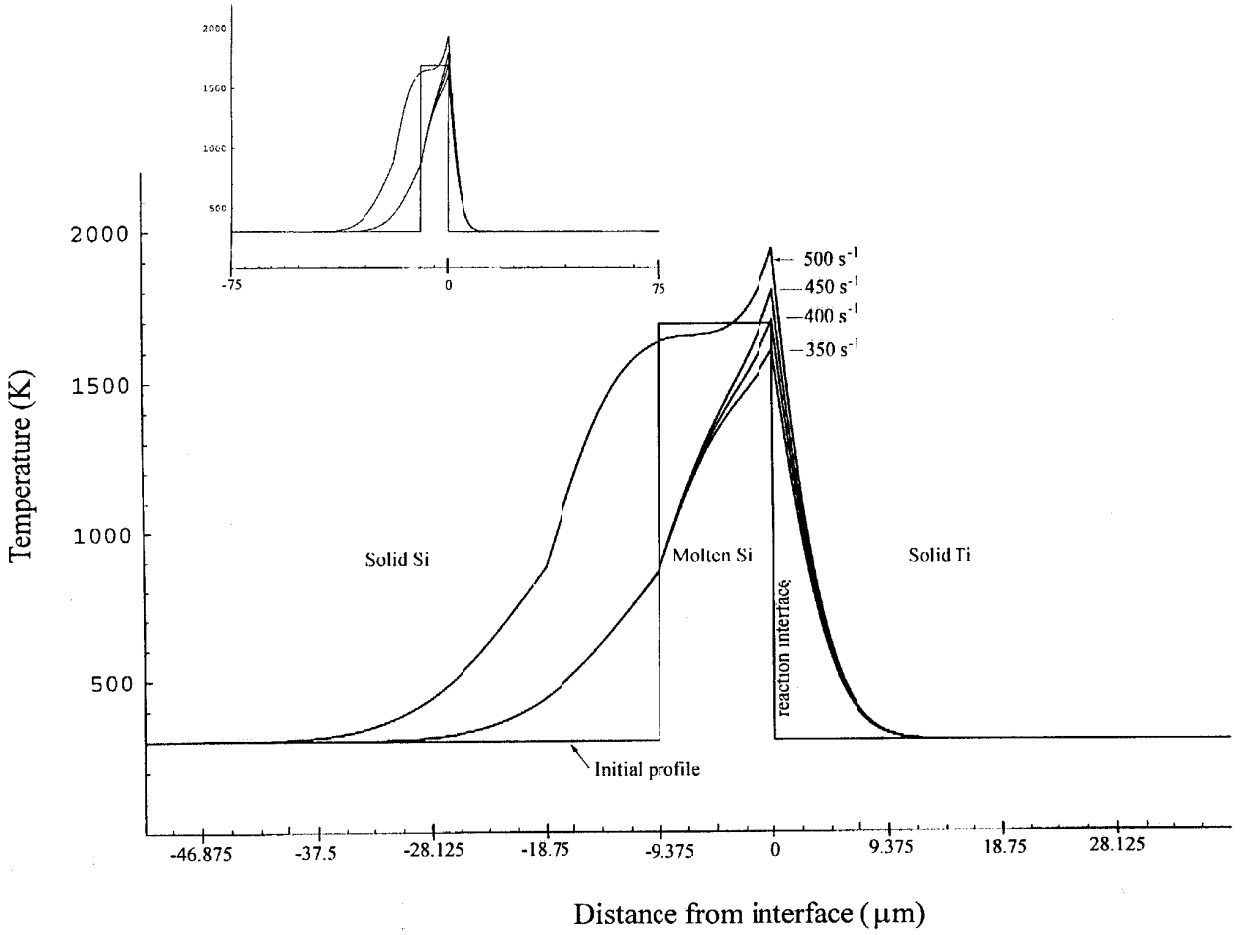

Figure 3.19 Temperature profile after 9 ns for increasing reaction rates.

References:

1. D.M. Shah, D. Berczik, D.L. Anton, R. Hecht, *Mat. Sci. and Eng.*, **A155**, p. 45 (1992).

2. B.R. Krueger, A.H. Mutz and T. Vreeland, Jr., *Met. Trans.*, **23A**, p. 55 (1992).

3. N.N. Thadhani, *J. Appl. Phys.*, **76**, p. 2129 (1994).

4. E. Dunbar, R.A. Graham, G.T. Holman, M.U. Anderson, and N.N. Thadhani, in *Proc. of AIRAPT/APS High Pressure Science and Technology Conference*, edited by C.S. Schmidt, Colorado Springs, CO, 28 June-2 July, 1993.

5. N.N. Thadhani, E. Dunbar, and R.A. Graham, *in Proc. of AIRAPT/APS High Pressure Science and Technology Conference*, edited by C.S. Schmidt, Colorado Springs, CO, 28 June-2 July, 1993.

6. F. Bordeaux and A.R. Yavari, *J. Matter. Res.*, **5**, p. 1656 (1990).

7. T. Vreeland, Jr, K.L. Montilla and A.H. Mutz, *J. App. Phys.*, **82** (6), p. 2840 (1997).

8. K.S. Vecchio, Li-Hsing Yu, M.A. Meyers, *Acta Metall. Mater.*, **42** (3), p. 701 (1994).

9. MA. Meyers, Li-Hsing Yu, K.S. Vecchio, *Acta Metall. Mater.*, **42** (3), p. 715 (1994).

10. P. Kasiraj, T. Vreeland, R.B Schwartz and T.J. Ahrens, *Acta. Metall.*, **32**, p. 1235 (1984).

11. R.A. Graham," Solids Under High-Pressure Shock Compression," Springer-Verlag (1992).

12. A. H. Mutz, "*Heterogeneous Shock Energy Deposition in Shock Wave Consolidation of Metal Powders*, " Ph.D. Thesis, Caltech, 1991

13. B. Krueger and T. Vreeland, Jr, *J. App. Phys.*, **69** (2), p. 720 (1991).

14. S.B. Bhaduri, Z. B. Qian and R. Radhakrishnan, *Scripta Met. et Mater.*, **30**, p. 179 (1994).

15. T.B. Massalski, J.L. Murray, L.H. Bennet and H. Baker, "Binary Phase Diagrams," American Society for Metals, Metals Park, OH (1986).

16. G.S. Cole, "Solidification," p. 201 Am. Soc. Metals, Metal Park, OH 1971

17. H.E. Boyer and T.L. Gal, "ASM Metals Handbook," American Society of Metals, Metals Park, Ohio (1980).

18. M.A. Meyers, S.S. Batsavov, S.M. Gavrilkin, H.C. Chen, J.C. LaSalvia, F.D.S. Marquis, *Mat. Sci. and Eng.*, **A201**, p. 150 (1995).

19. N. N. Thadhani, *Prog. Mat. Sci.*, **37**, p. 117 (1993).

20. R.B. Schwartz, P. Kasiraj, T. Vreeland and T.J. Ahrens, *Acta Metall.*, **32**, p. 1243 (1984).

21. H.B. Chen, V.F. Nesterenko, and M.A. Meyers, UCSD/IMM Report No. 97-9 (1997).

22. P.A. Taylor, M.B. Boslough, and Y. Horie, in "Shock Waves in Condesed Matter," edited by. S.C Schmidt, N. C. Holmes (Elsevier Science Publishers B.V., 1987).

23. W. Tong and G. Ravichandran, *J. App. Phys.*, **74** (4), p. 2425 (1993).

24. J.J. Moore, D.W. Readey, H.J. Feng, K. Monroe, and B. Mishra, *JOM*, (Nov. 1994).

25. R. Radhakrishnan, S. Bhaduri and C. H. Henager, Jr., *JOM*, (Jan. 1997).

26. L.H. Yu and M.A. Meyers, *J. Mat. Sci.*, **26** , p. 601 (1991).

27. S. C. Deevi and N.N. Thadhani, *Mat. Sci. and Eng.*, **A192/193**, p. 604 (1995).

28. H.C. Chen, M.A. Meyers, and V.F. Nesterenko,in *Metallurgical Application of Shock-Wave and High-Strain-Rate Phenomena*, edited by L. E. Murr, K.P. Staudhammer, and M.A. Meyers (Dekker, New York, 1995), p. 723.

29. J.C. La Salvia and M.A. Meyers, *Met. and Mat. Trans.*, **26A**, p. 3011 (1995).

30. J.C. LaSalvia, D.K. Kim, R.A. Lipsett, and M.A. Meyers, *Metall. and Mater. Trans.*, **26A**, p. 3001 (1995).

31. A.N. Dremin and O.N. Breunov, *Russian Chem. Rev.*, **37**, p. 392 (1968).

32. K. Blathe, "Finite Element Procedures in Engineering Analysis," Prentice-Hall, 1982

33. Y.S. Toulaukian, "Thermophysical Properties of Matter. v1: Thermal Conductivity - Metallic Elements and Alloys," New York - Washington, IFI/Plenum, 1970

33. Y.S. Toulaukian, "Thermophysical Properties of Matter. v1: Thermal Conductivity - Metallic Elements and Alloys," New York - Washington, FI/Plenum, 1970

34. V. F. Nesterenko, M.A. Meyers, H.C. Chen, J.C. LaSalvia, *Appl. Phys. Lett.*, **65**, p. 24 (1994).

CHAPTER 4. The Mo + 2 Si System

4.1 Background

Although $MoSi_2$ had been available since the early nineteen-hundreds when it was used in Germany as a corrosion-protective coating for ductile metals, it was not commonly accepted in the United States until the late nineteen-forties, when A.W. Maxwell suggested its use for structural applications [1,2]. Maxwell documented its strength, creep resistance, and thermal shock behavior at elevated temperatures. However, due to its room temperature brittleness, research efforts were not continued. It was not until twenty years later when silicides were being considered as coating materials for gas turbine engines that $MoSi_2$ reemerged as a structural material [2].

Research conducted at Los Alamos National Laboratories was pivotal in attracting the attention of the aerospace industry in the late nineteen-eighties. This interest was driven by the need to develop materials for advanced applications that could operate at high temperatures (~ 1400 K). Silicides are unique in their ability to provide a silica layer upon high temperature oxidation. Of the silicides, $MoSi_2$ is an exceptional candidate due

to its high melting point (2293 K), high modulus (440 GPa), relatively low density (6.31 g/cm^3), and the ability to withstand high operational temperatures (up to 1700 ^oC) [2,4].

Its widespread use has been limited due to poor room temperature ductility and high temperature creep. The $MoSi_2$ brittle-to-ductile transition temperature (BDTT) is at 1000 ^oC; above this temperature it becomes ductile [3]. Unfortunately, this increase in ductility is accompanied by a significant decrease of strength. Efforts to enhance its mechanical response must include improvement of both low temperature ductility and high temperature strength.

The creep resistance can be greatly improved by the addition of SiC resulting in a composite with high fracture toughness. Consequently, another attractive property of $MoSi_2$ is its thermodynamic stability with many technologically advanced ceramic reinforcements [4]. Alternatively, $MoSi_2$ can be alloyed with other silicides to improve its overall properties. The viability of $MoSi_2$ as an ideal matrix for high temperature intermetallic composites is well documented [4,5].

This chapter describes the efforts to produce dense $MoSi_2$ compacts via shock wave consolidation and mechanical ball milling. Mechanical alloying and shock wave consolidation are viable alternatives for the synthesis and consolidation of $MoSi_2$. In this study, mechanical alloying of $MoSi_2$ is performed by ball milling Mo + 2Si powders at room temperature in an argon

environment. The mechanical alloying of $MoSi_2$ is monitored with X-ray diffractometry and differential thermal analysis (DSC). The as-received powder mixture (Mo + 2Si) is shock consolidated to produce $MoSi_2$.

4.2 Powder Processing of $MoSi_2$

Powder metallurgy techniques have been used extensively in silicide production [1-3,6]. These methods often consist of pre-alloyed powders of the silicide system followed by densification. Hot isostatic pressing in the range of 1100 ^oC to 1500^o C is a standard method. Other processing methods include self-propagating high temperature synthesis, spray processing, solid-state displacement reactions (i.e., diffusional phase transformations) and exothermic dispersion (XD^{TM}) [8].

Mechanical alloying of molybdenum disilicide was initially introduced in an attempt to minimize oxygen contamination, which is common during conventional processing techniques. During synthesis, oxygen combines with silicon to form SiO_2. The formation of the glassy oxide SiO_2 precipitates at the $MoSi_2$ grain boundaries results in the degradation of mechanical properties, especially at high temperatures. The oxide appears to reduce the fracture strength of the material as evidenced from scanning electron microscopy (SEM) of the fracture surface in which intergranular fracture is observed [3]. Incidentally, the formation of this silica at the surface of the silicide results in excellent corrosion and oxidation resistance of $MoSi_2$.

The source of the SiO_2 is believed to be the powder surfaces in contact with air during powder grinding, prior to the arc melting or sintering process. It has been proposed that mechanical ball milling could be performed under a high purity argon atmosphere to greatly reduce the oxygen content. In addition, due to the fine particle size of the mechanically alloyed powders, hot-pressing could be accomplished at a much lower temperature than that of commercially available powders. Ball milled powders could be hot pressed at 1500 ^{o}C versus 1800 ^{o}C for commercially available powders [3]. This reduction in temperature plays a major role in the reduction of SiO_2, since 1500 ^{o}C is well below the softening temperature for the silica (~1650 ^{o}C). This process is very successful in reducing the oxygen content in the silicide.

Another problem that arises during the synthesis of $MoSi_2$ is a high level of porosity. This porosity results from the melting of Si and molar volume difference between $MoSi_2$ and Mo+2Si. Thus, the application of pressure at or above the melting point of silicon is essential to eliminate the porosity. The highest density achieved is approximately 99.2% by field-activated combustion synthesis. The process incorporates the application of pressure on the reactants under vacuum conditions, the imposition of an electric current in a pulsed mode, the continuous imposition of a current until the target temperature is reached, and the cooling of the product at a constant rate [4].

4.3 Grain Size Effect

In addition to the reduction in processing temperature, the grain size of the powders after mechanical ball milling is significantly reduced. Grain size refinement is desirable to improve the yield strength of the material. It is well known that the yield strength of materials increases with decreasing grain size since grain boundaries act as barriers to the motion of dislocations [9]. This relationship known as the Hall-Petch equation results in an inverse square root dependence of yield strength with grain size:

$$\sigma_y = \sigma_o + \frac{k}{\sqrt{d}} \tag{4.1}$$

where, σ_y, σ_O, d and k are yield stress, frictional stress, grain size and a positive material constant, respectively. Although recent studies have put into question the validity of this relationship for nanocrystalline materials, it has since been established that the strength of nanocrystalline solids increases with decreasing grain size [10].

4.4 Experimental Procedure

The molybdenum and silicon powder mixture utilized in this investigation is obtained from Oak Ridge National Laboratory, Oak Ridge, TN. The nominal particle sizes for the molybdenum and silicon are 3.4 μm and 6.1 μm, respectively. The powder mixture had a stoichiometric composition of Mo + 2 Si. The $MoSi_2$ compound exhibits two equilibrium structures: a low temperature body-centered tetragonal structure; and a high temperature hexagonal structure. The phase transition between the tetragonal and hexagonal structure occurs at 1850 ^oC. A phase diagram of the

Mo-Si system is provided in Figure 4.1 with the composition of interest labeled [11].

4.4.1 Mechanical Ball Milling

Mechanical alloying entails the repeated welding, fracturing and rewelding of powders during high-energy milling. The process is schematically illustrated in Figure 4.2 where, the first step is an intense cold welding period. Followed by a rapid fracturing period forming lamellae. The production of finer and more convoluted lamellae results from a moderate cold welding period. The process is completed by a steady-state period [8]. In addition, repeated particle impact at contact points leads to local hot spots.

Ball milling is performed in hardened steel vials with a 1:5 ratio by weight of powders to hardened steel balls. Two different sizes of steel balls (a large 1/2" and small 1/4" diameter) are used. Eight balls of each size are used with a total weight of 76 gms (for 15 gms of powder). The powders are packed in an argon glove box to reduce oxygen contamination during mechanical ball milling. A SPEX 8000 shaker mill is used to ball mill the powders.

The duration of ball milling is increased from 2 hours to 144 hours. After each time interval a small amount of powder is removed to examine the grain size by x-ray diffraction (XRD). An Inel diffractometer with a CPS120 curved detector unit is used to collect XRD diffraction patterns [12,13]. This system operates using a Co Kα radiation (λ = 1.7902 A) and a curved position sensitive detector with a 250 mm radius and a 120^{o} window. The detector is

electronically programmed to scan in steps of approximately 0.03°. The curved gaseous detector is designed around a blade anode in flowing mixture of 15% Ethane and 85% Argon gas. The incident beam is focused onto the detector by a bent quartz-crystal monochromator. The detector slit system is adjusted to accept only Co Kα radiation from the sealed X-ray tube.

4.4.2 Consolidation Ball Milled Powder

The shock wave consolidation experiments are performed in the Keck Dynamic Compaction Laboratory . This facility operates with propellant driven stainless steel flyer plates in a 3 meter long by 35 millimeter in diameter smooth bore launch tube. A 5 mm thick flyer plate is carried by a nylon sabot and strikes the powder directly without striking the powder containment fixture (Figure 4.3). This assembly results in a well controlled plane-wave geometry [14]. There are a number of assembly parameters that can be adjusted to aid in the recovery of a good compact (i.e., non-porous, crack-free), including initial powder depth, flyer plate thickness, and flyer plate velocity.

The powder is packed into a cylindrical powder cavity and leveled. The powder is then pressed quasi-statically to the desired porosity using an Instron 4204 Universal Testing Machine. For a porosity of approximately 44% a 7,000 lb. load is required. For this study, the porosity is held constant for all the experiments at 44%. The pressed powder depth for each experiment is approximately 15 mm. The target is sealed to the barrel to the left by an extension assembly, which houses the velocity instrumentation, and to the

right by a momentum trapping assembly (Figure 4.3). The velocity instrumentation consist of two pairs of fiber optic cables which plug into the barrel extension. The fiber optic cables form a closed loop with one pair of cables serving as light sources and the other pair as receiver cables. Each light source is focused across the barrel extension onto the receiving fiber optic cable. A tungsten filament lamp is used as the light source. When the first light source is interrupted it sends a signal to the counter to start and the second light interruption stops the counter. From the total time and the distance between the light sources (4.0 cm), the velocity of the flyer plate can be calculated.

Before each experiment the barrel is evacuated, back filled with argon, and evacuated again to remove any residual oxygen. The barrel is evacuated through a connection to the barrel extension. The final vacuum in the barrel for an experiment is about 0.25 torr. The recovery chamber is also evacuated by a separate vacuum pump for safety and noise control. Earlier studies have shown that the reaction can be triggered at a much lower shock energy in the presence of oxygen in other silicide systems [15].

After each experiment, visual observations of the recovered compact are useful in determining the extent of reaction within the compact. The first experiment is performed on the as-received powder mixture at a relatively low shock energy (273.3 J/g). The powder is fully consolidated with the appearance of localized reaction zones. However, the reaction did not

propagate to completion within the compact. This shock energy is below the threshold energy needed to sustain the reaction.

The next experiment is conducted at a higher shock energy, 445 J/g. This is a multi-cavity shot. A divider is used to separate four different powder mixtures within the powder cavity of the target holder. The divider is used only for the loading and initial pressing of the powders and is removed prior to shock consolidation. This assembly has been shown to be consistent with plane-wave approximations. The other powder mixtures included Fe + 2 Si, Ni + 2 Si, and a Mo + Si + C. Visual observations indicate that the sample of Mo + 2Si is completely reacted. The sample is riddled with shrinkage voids, which is indicative of rapid solidification. Figure 4.4 is a Backscattered SEM micrograph of the recovered compact. The sample is extremely porous.

A full cavity shot of the Mo + 2 Si mixture is performed at the same shock energy of the multi-cavity shot, 445 J/g. The recovered compact is fully reacted with a numerous shrinkage voids throughout the cross-section. The sample is sectioned using a high-speed diamond saw. A representative cross-section is mounted in epoxy and mechanically polished. Optical microscopy confirmed full reaction and profuse void formation.

4.5 Experimental Results

4.5.1 DSC Analysis

Differential scanning calorimetry (DSC) is utilized for the thermal analysis of the powders. DSC is used to monitor the onset of endothermic and exothermic reactions, peak temperatures, and the number of reactions. The DSC analysis is performed at the Oak Ridge National Laboratory. Samples of the as-received powder mixture and samples of the ball milled powders at the various milling intervals are examined. The DSC analysis of the as-received powder mixture exhibited a strong endotherm at 1383 ^{o}C, which is just below the melting temperature, 1412 ^{o}C, of Si (Figure 4.5). The DSC scan of the powder after two hours of ball milling is illustrated in Figure 4.6. The onset of the endotherm is found at 1278^{o}C, over 100^{o} C degrees below that exhibited by the as-received powder. The reduction in temperature is a result of the close intimate mixing and reduction in grain size achieved through ball milling. The continuous fracturing and cold welding of the particles during ball milling ultimately leads to alloying on the atomic level.

The four-hour ball milled sample exhibited an exotherm at approximately 600 ^{o}C. This is over 800 ^{o}C below the melting temperature of Si. The DSC scan for the four-hour ball milled sample is plotted in Figure 4.7. This reduction in reaction temperature is due to the increased contact area between the silicon and molybdenum and the creation of fresh, clean surfaces generated by ball milling. The sample ball milled for sixteen hours did not

exhibit an exotherm, as can be seen from its DSC scan plotted in Figure 4.8. It is likely that the silicide formation is completed during the sixteen hours interval. Hence, there is no energy release from the negative heat of formation of the silicide. Self-sustained exothermic reactions leading to $MoSi_2$ formation during room-temperature high-energy ball milling of elemental powders has been documented by Ma et al. [16].

4.5.2 X-ray Analysis

Figure 4.9 is the XRD data collected from the powder after two hours of ball milling. All the diffraction peaks have been identified as either pure Mo or Si. Thus, we can conclude that after two hours of ball milling no reaction has occurred. The diffraction peaks for the eight-hour ball milled powder are identical to those of the four-hour ball milled powder, with the exception of additional peak broadening for the eight-hour sample. Figure 4.10 is the XRD data collected from the four-hour ball milled powder sample. The silicide reaction has been initiated during ball milling. There is a both tetragonal and hexagonal $MoSi_2$ with some pure Mo. The pure Mo peaks have also been observed by Schwartz et al. and Zhang [3,18]. The tetragonal phase appears to be in greater abundance, which is expected since it is most likely to form first. It has the largest negative heat of formation of all the equilibrium molybdenum silicides [18]. As the milling time is increased the amount of the tetragonal phase appears to increase while that of the hexagonal and pure molybdenum decreases. This trend is evident from Figure 4.11, where the XRD data for the twenty-four-hour ball milled powder is plotted.

These results are consistent with those obtained by Zhang, who investigated the role of the Si composition on phase formation behavior during mechanical alloying of Mo and Si powders. After ball milling a mixture of Mo + 2 Si for four hours, both the tetragonal and metastable hexagonal $MoSi_2$ where present as evidenced by x-ray diffraction patterns [18]. He also found that as the atomic percentage of Si is decreased in the starting powder, different phase formation behavior is observed during milling. No formation of the silicide is observed after decreasing the Si to 25 % at. wt. for a mechanical ball milling interval of thirty-six hours.

XRD data of powder sample from the shock consolidation experiments are also obtained. The diffraction peaks for shot #178 (shock consolidated as-received powder sample) is similar to the as-received powder and the two-hour milled sample. This sample is shocked below the threshold shock energy for reaction initiation and no reaction is observed in the recovered sample. The peaks are those of pure Mo and pure Si. The XRD data for shot 178 is plotted in Figure 4.12.

For shot #180 (the multi-cavity shot), the recovered sample appears to have undergone complete reaction. The XRD data for this sample is provided in Figure 4.13 which points to the formation of the $MoSi_2$ silicides. The peaks for this sample are not labeled, but the XRD patter for the twenty-four hour ball milled powder is provided for comparison. The two XRD patterns are similar, with the exception of peak broadening for the ball milled powder. Most of the silicide exhibits the high temperature hexagonal structure.

During reaction synthesis the temperatures are expected to be well above 1850 ^{o}C, which is the transformation temperature between the tetragonal and hexagonal structure.

4.5.3 Grain Size Determination

From the x-ray diffraction data, it is observed that as the milling time is increased, the initially sharp peaks begin to broaden. This is known as grain size broadening of the peaks, and is a clear indication of grain size reduction and increasing strain at the atomic level. Figure 4.14 is a plot of grain size broadening as a function of ball milling times which clearly shows the grain size refinement for the silicide. The as-received and the 2 hour ball milled sample are not shown since the diffraction peaks are different (i.e., those of pure Mo and Si). The grain size distribution is computed from standard methods using the full width at half maxima (FWHM) of the peaks. This method separates the effects of grain size refinement from those of atomic level strain [19]. The approximations of size broadening profiles by Cauchy function is supported by both theory and experiment [19,20].

The grain size distribution for each milling time is listed in Table 4.2 and plotted in Figure 4.15. Initially, there is a large reduction in grain size for relatively short ball milling times. But after about twenty-four hours, the grain size refinement levels off. The grain size for the one hundred and forty-four-hour ball milled powder is not calculated.

The powder morphology and grain size for the different ball milling intervals are also examined by transmission electron microscopy (TEM). The

nanocrystalline size of the $MoSi_2$ silicide is confirmed by TEM images corresponding to the sixteen-hour and hundred and forty-four ball milled powder. Figure 4.16a is a TEM micrograph of the 16 hour mechanically ball milled powder. It has been reported that ball milling produces extensive dislocation densities that precipitate to form dislocation cell walls and form nanograin boundaries [16]. A uniform distribution of nano-sized grains is evident from this microgragh as well as Figure 4.16b, after hundred and forty-four hours of ball milling.

4.5.4 Shock Consolidation Results

Visual observations of the recovered compact after shock consolidation are useful in determining the extent of reaction within the sample. For the experiments performed either a flaky powder or porous solid is recovered. The profuse porosity within the compact is indicative of melting and rapid solidification. A Camscan series 350 scanning electron microscope (SEM), equipped with a LINK analytical energy dispersive X-ray spectrometer (EDS), is utilized to identify the reaction product and evaluate the extent of the porosity. Scanning electron microscopy along with the EDS analysis of this sample indicates that reaction proceeded to completion. Figure 4.4 is a Backscattered SEM micrograph of the sample. The silicide product exhibited significant porosity.

These results indicate that the shock energy is above the threshold shock energy for the reaction as proposed by Krueger et al. [15]. This condition requires that the calculated homogeneous temperature must be in excess of

that required to initiate the reaction in unshocked powder mixtures. This threshold shock energy condition has since been modified by Meyers et al., who consider the effect of shock pressure and plastic strain on chemical reactions in the Mo-Si system [22]. Specifically, the role of plastic deformation on the initiation of the chemical reaction is examined. They suggest that the threshold energy condition should take into account the plastic deformation energy.

Meyers et al. have outlined a mechanism for reaction growth for the Nb-Si and Mo-Si systems [22]. It is proposed that initially silicon melts while molybdenum remain in the solid state. The molten intermetallic grows by the dissolution of the molybdenum into the liquid silicon. They attribute capillary effects to the formation of spheroids (with the silicide composition), which subsequently solidify and are expelled into the liquid silicon. A high reaction rate is maintained throughout the extent of the reaction by the constant renewal of fresh solid molybdenum-liquid silicon interface. The reaction proceeds to completion until one of the constituents is entirely consumed.

4.6 Conclusions

High energy ball milling is a viable technique for grain size refinement of the Mo + 2 Si powder mixture. A milling time of sixteen hours is required to obtain fully alloyed $MoSi_2$. The grain size refinement is complete after 24 hours of ball milling. After two hours of ball milling, the melting temperature of Si is reduced by 100 °C from that of the as-received Mo + 2Si

powder mixture. Ball milling for four to eight hours results in a reaction exotherm at 600 °C. Nanocrystalline $MoSi_2$ is obtained after twelve hours of ball milling. The grain size refinement as a function of milling time is verified from the TEM micrographs of the sixteen-hour and the hundred forty-four-hour ball milled powders (see Figure 4.16).

Synthesis of $MoSi_2$ via shock wave consolidation is achieved. A shock energy of approximately 445 J/g is needed to initiate the silicide reaction within the elemental powder mixture. However, the porosity of the silicide product needs to be eliminated. To reduce this porosity, it may be advantages to dilute the exothermic energy release, in order reduce the amount of product melting. Since, the sixteen-hour ball milled sample did not exhibit an exotherm as evidenced from its DSC scan, it is probable that mixing some reacted ball milled powder with the elemental powder mixture can dilute the exothermic reaction within the as-received powder.

Table 4.1 Standard deviation in grain size with increase in milling time

Ball milling time	Grain size (nm)	Deviation (nm)
0	49.63	± 43.43 *
2	35.57	± 6.314
4	29.96	± 13.06
8	13.4	± 2.14
16	8.367	± 0.56
24	5.96	± 1.477
48	4.309	± 0.203

*This deviation is due to the large distribution of grain size in the as-received powder.

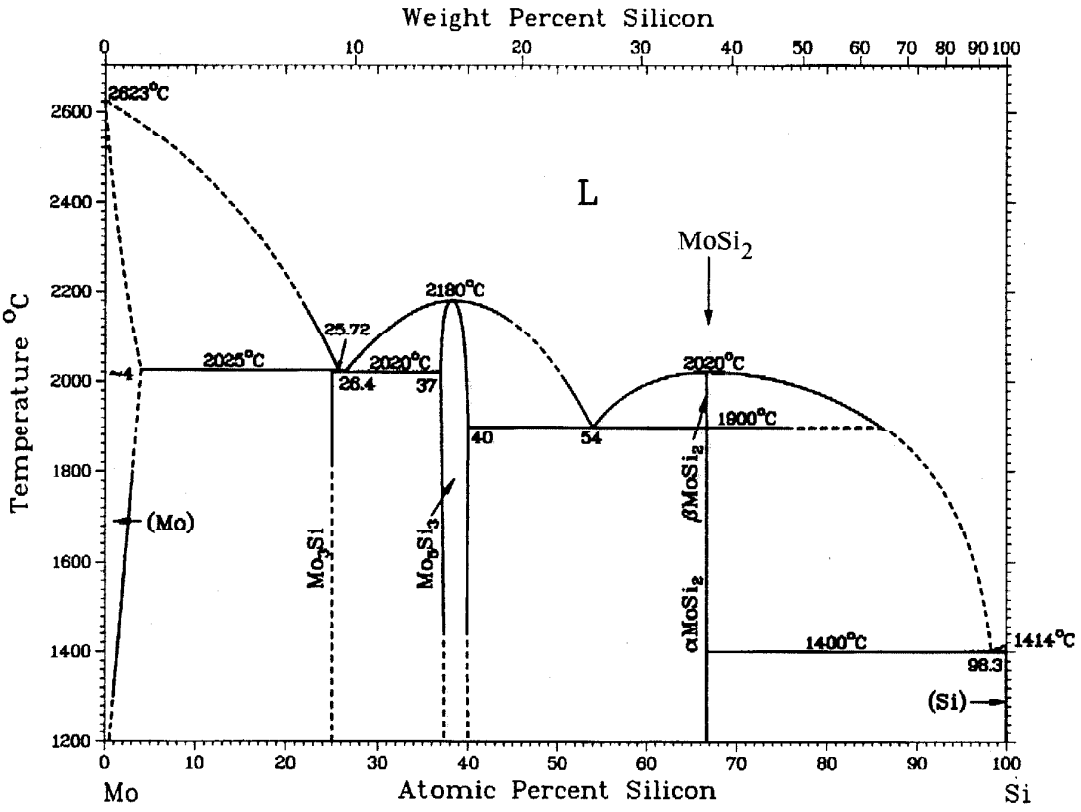

Figure 4.1 Binary phase diagram for Mo-Si system [11].

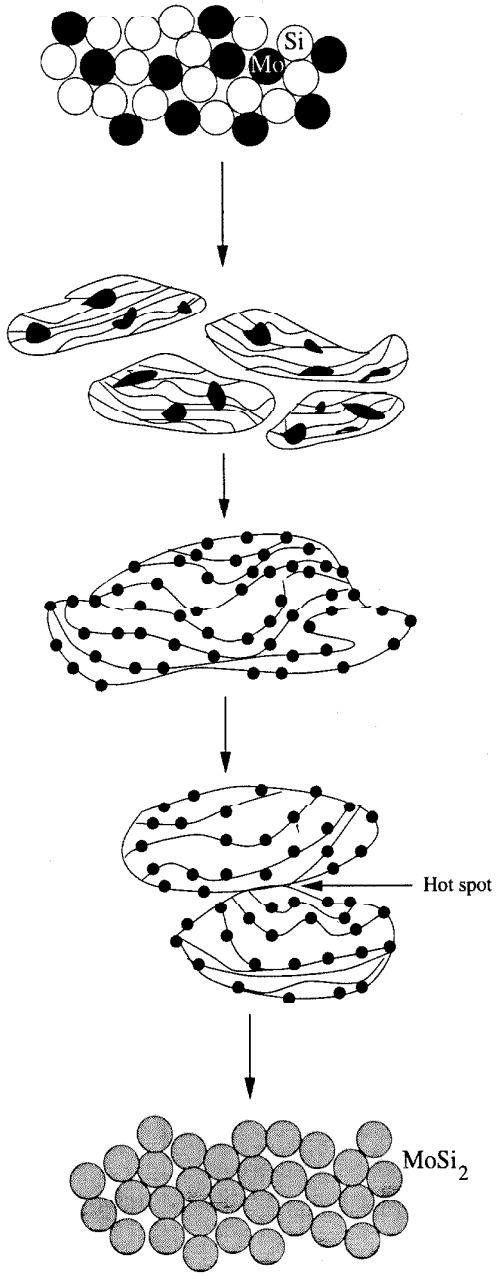

Figure 4.2 Schematic of $MoSi_2$ compound formation by mechanical ball milling [7].

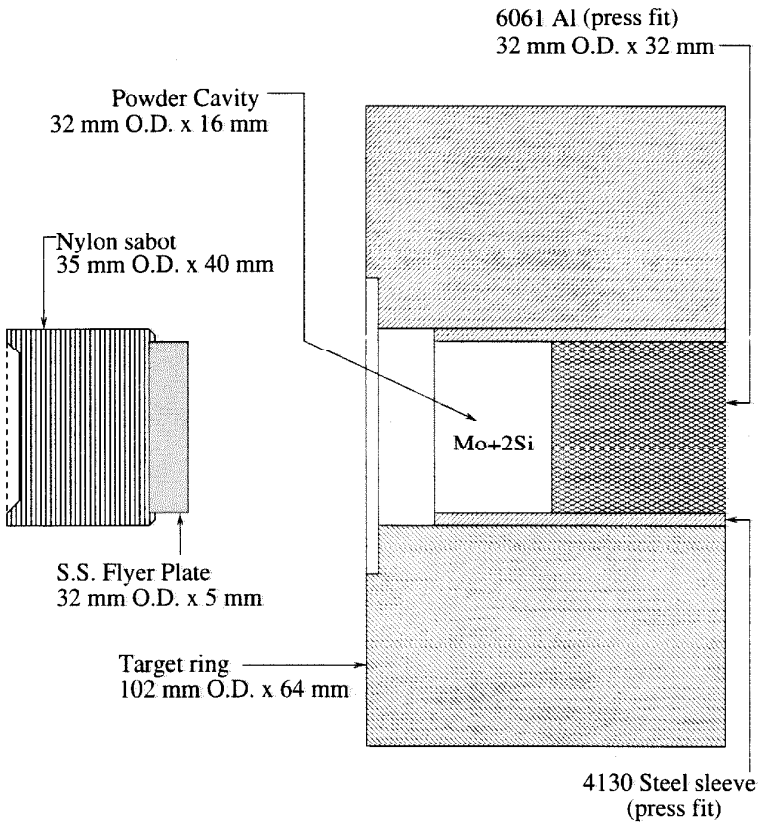

Figure 4.3 Schematic drawing of the sabot with flyer plate and target design.

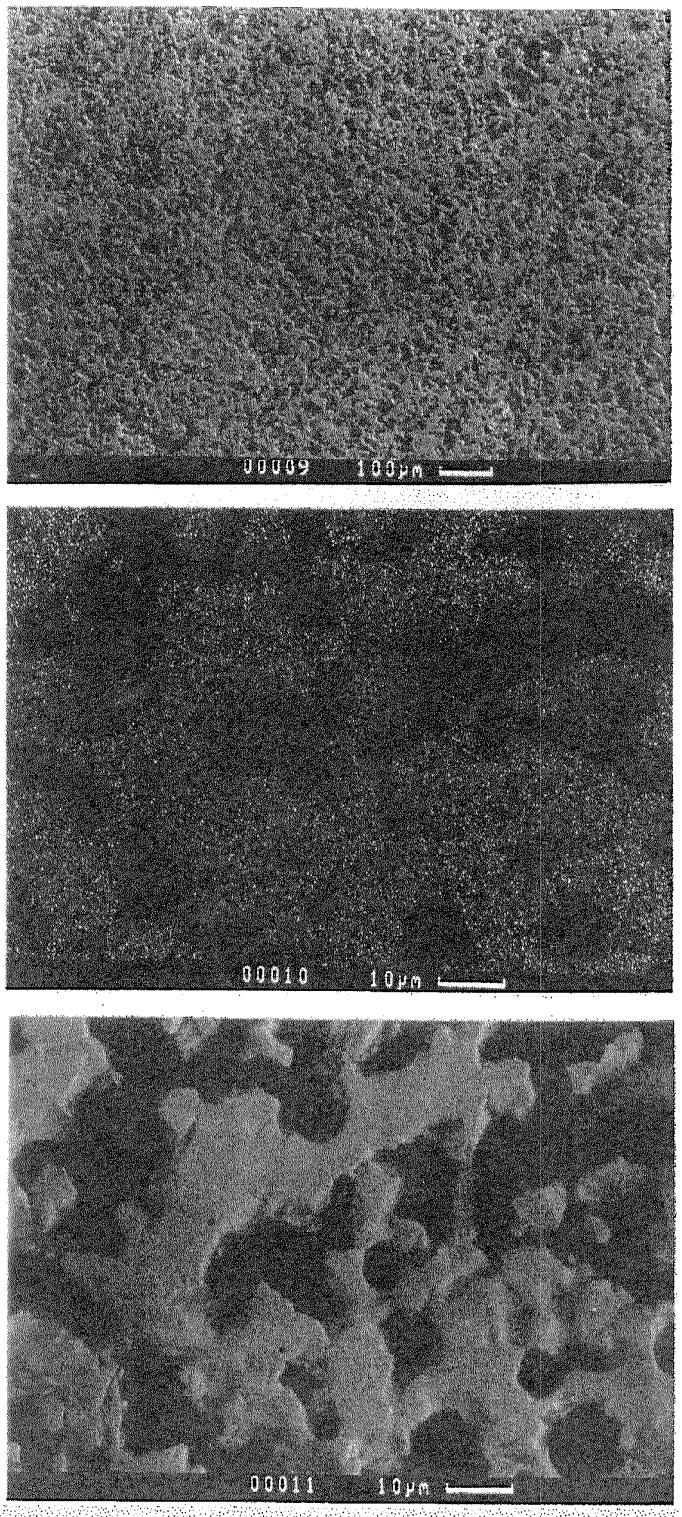

Figure 4.4 Backscattered Sem micrograph of reacted Mo + 2Si powder (Shot #180).

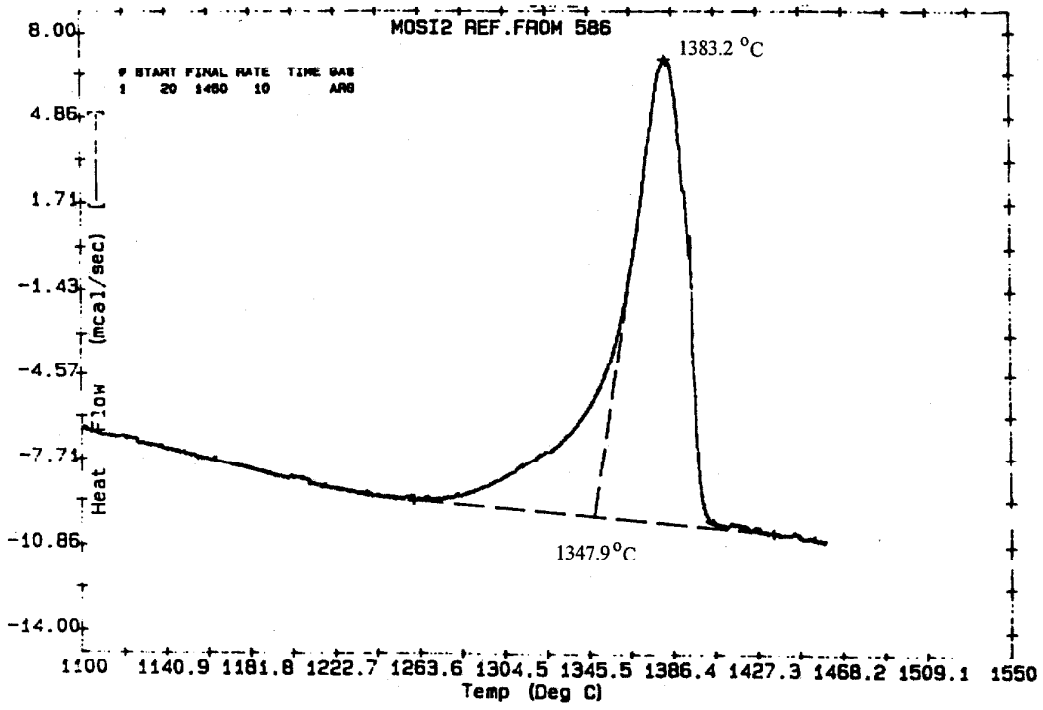

Figure 4.5 DSC scan for as-received Mo+2Si powder mixture.

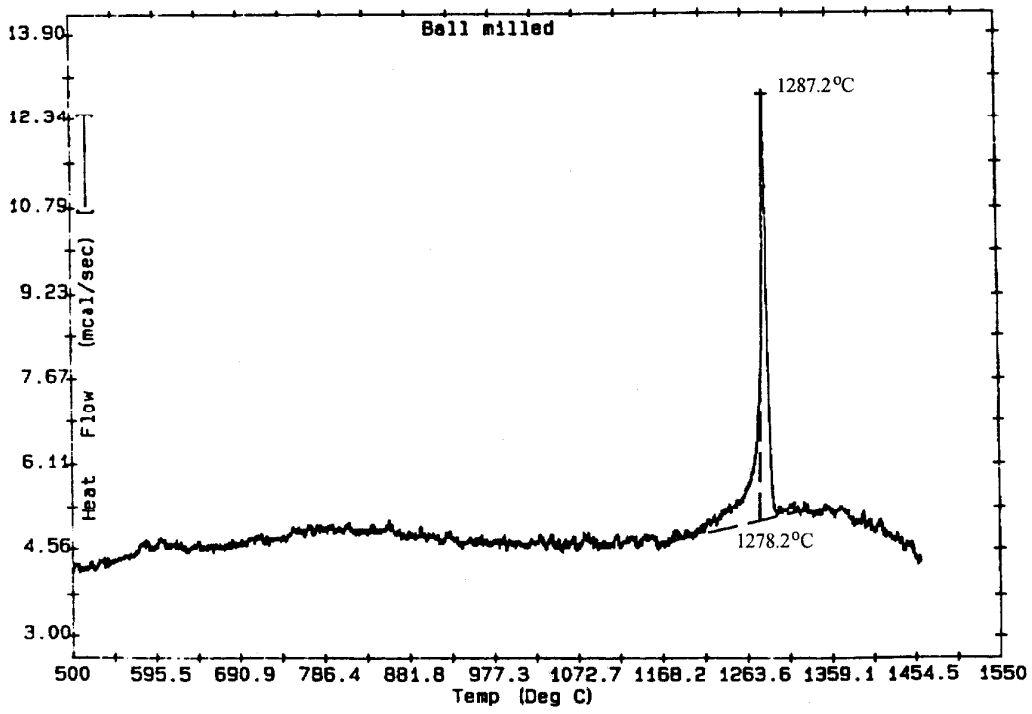

Figure 4.6 DSC scan for the 2 hour ball milled Mo+2Si powder.

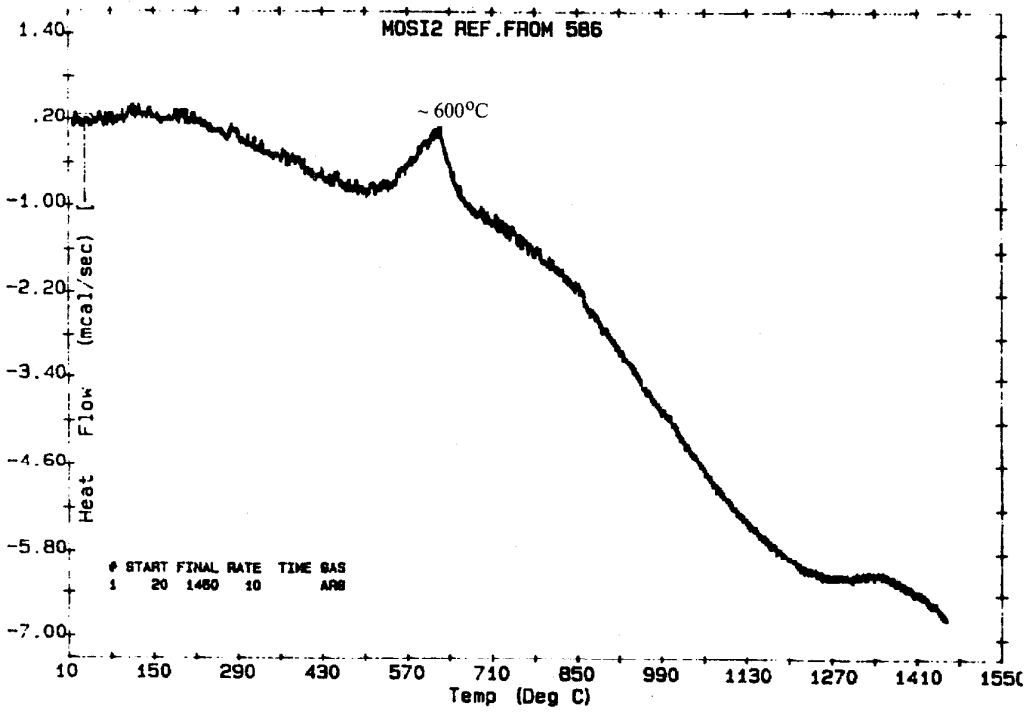

Figure 4.7 DSC scan for the 4 hour ball milled Mo+2Si powder.

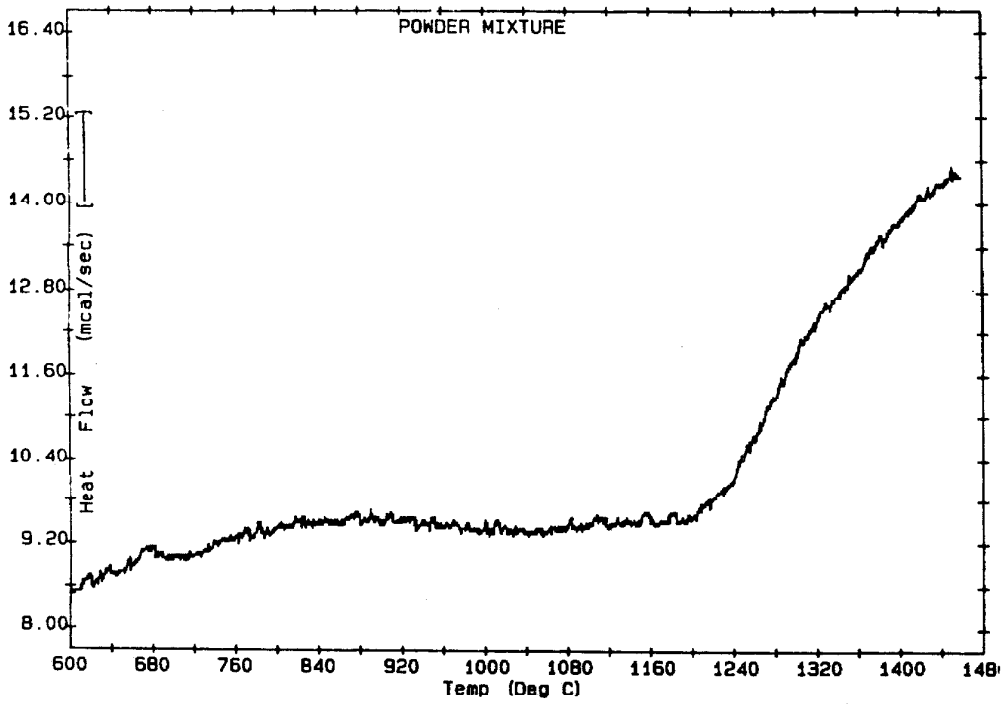

Figure 4.8 DSC scan for the 16 hour ball milled Mo+2Si powder.

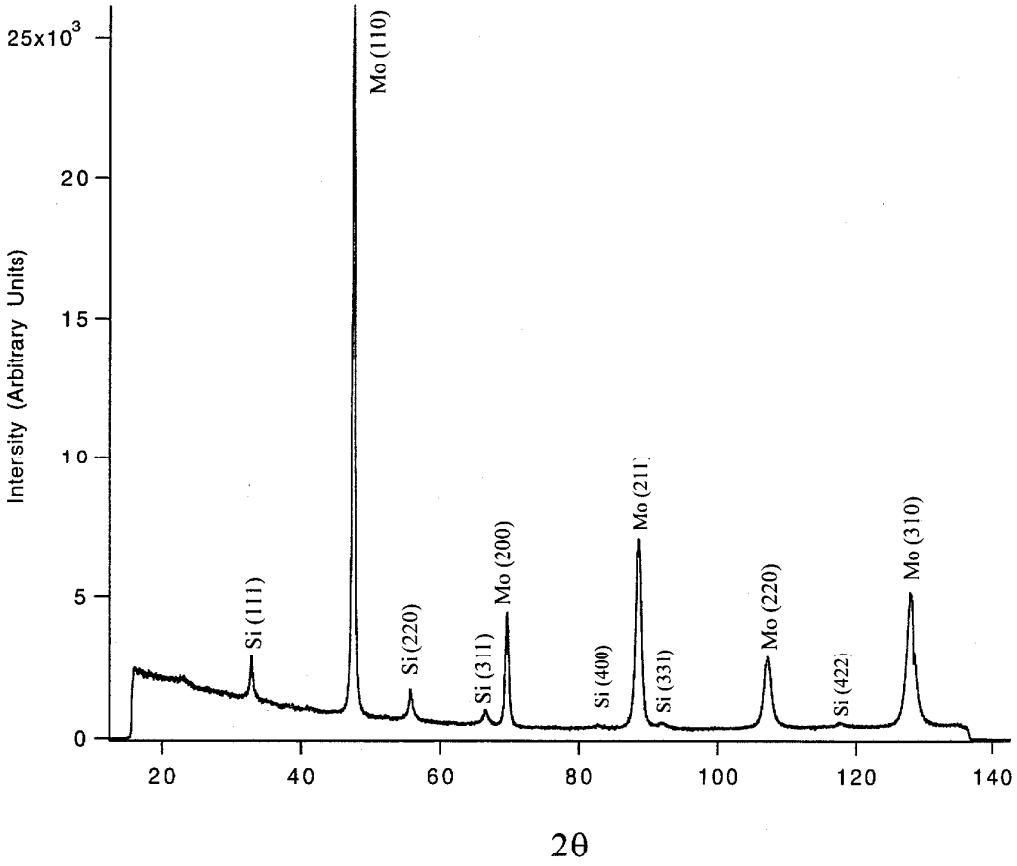

Figure 4.9 X-ray diffraction data for the 2 hour ball milled Mo+2Si powder. All peaks have been identified as either pure Si or Mo.

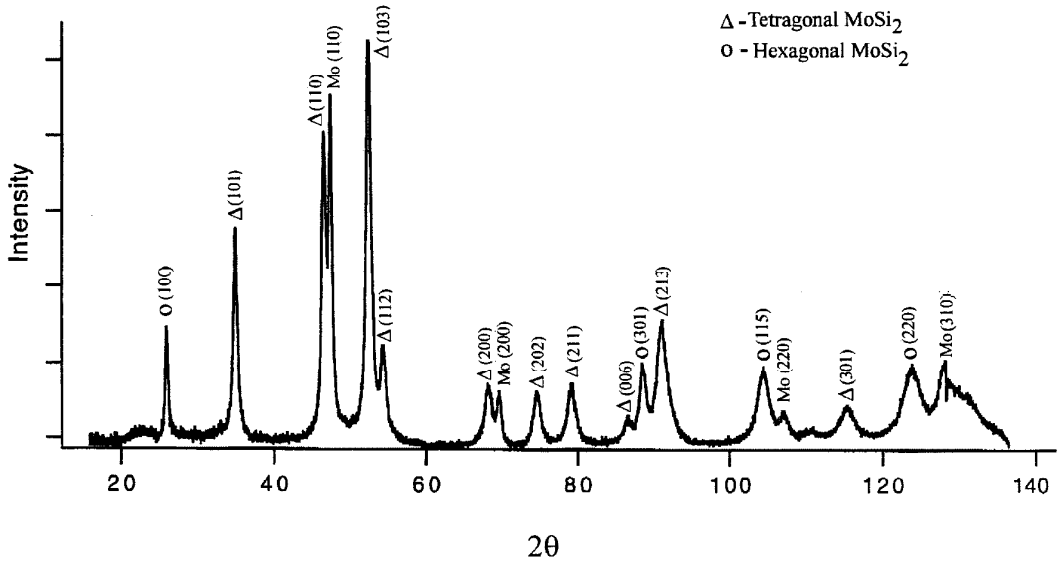

Figure 4.10 X-ray diffraction for the 4 hour ball milled Mo+2Si powder. Silicide formation has begun; small amount of pure Mo present.

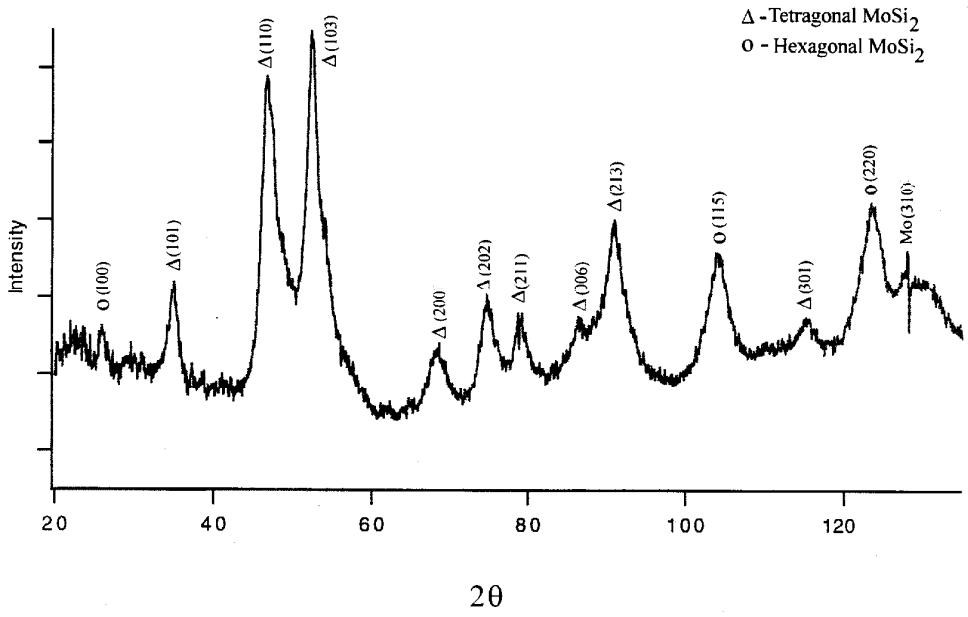

Figure 4.11 X-ray diffraction data for the 24 hour ball milled Mo+2Si powder. Silicide formation is complete.

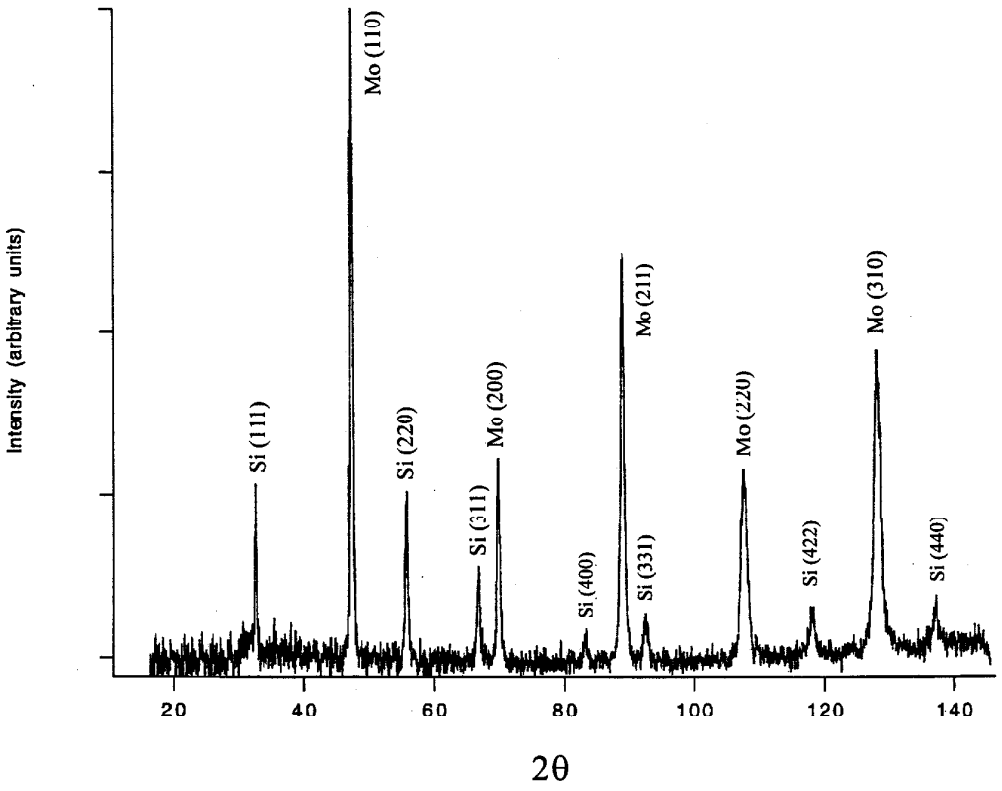

Figure 4.12 X-ray diffraction data for shot #178 (as-received powder). No reaction during shock wave consolidation process.

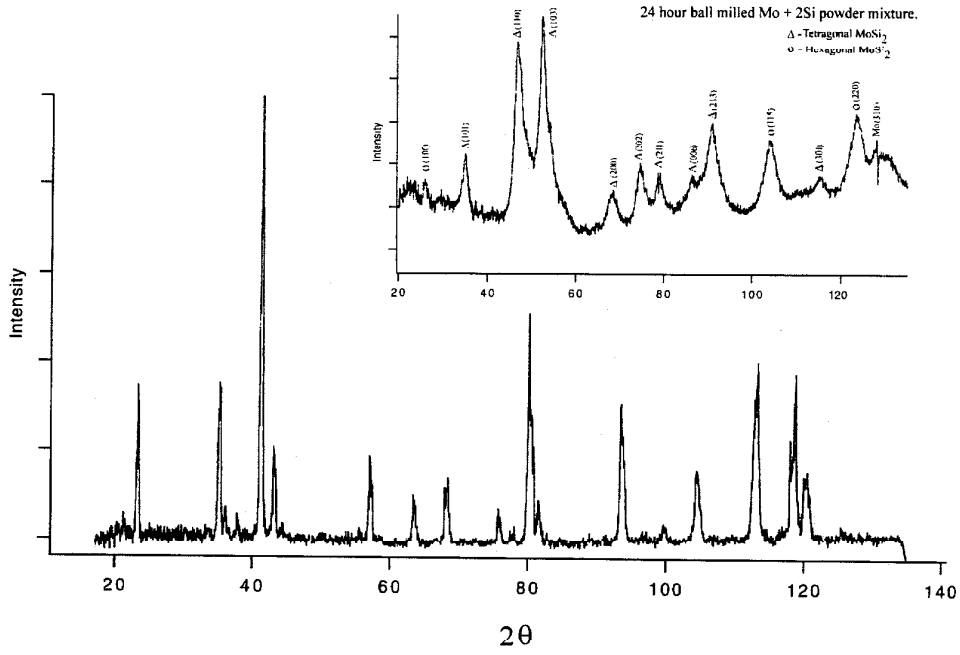

Figure 4.13 X-ray diffraction for shot #180 (Mo+2Si powder).
The sample appears fully reacted.

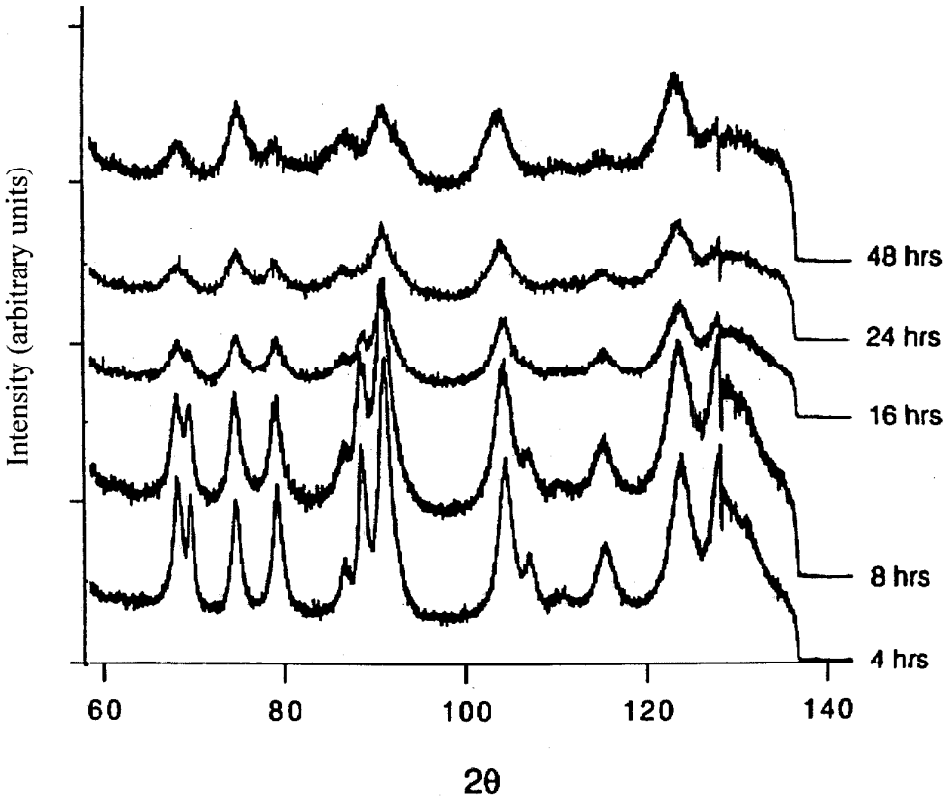

Figure 4.14 Grain size broadening indicated by XRD due to increased ball milling in $MoSi_2$.

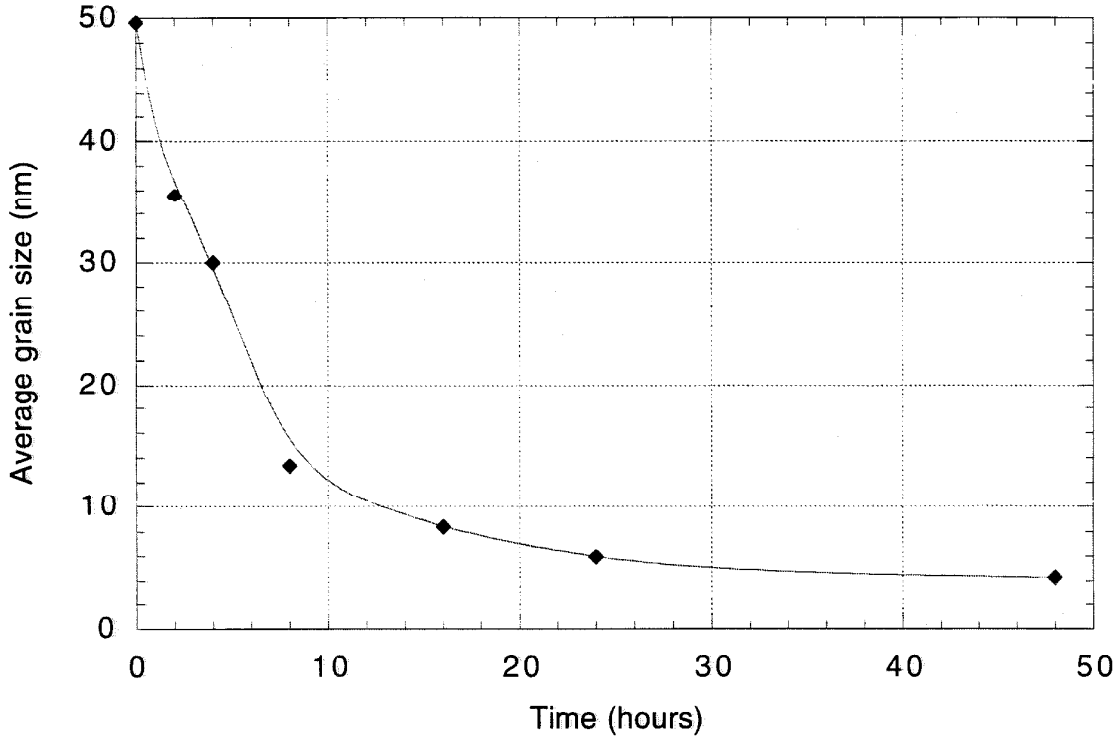

Figure 4.15 Average grain size vs ball milling time for Mo+2Si power.

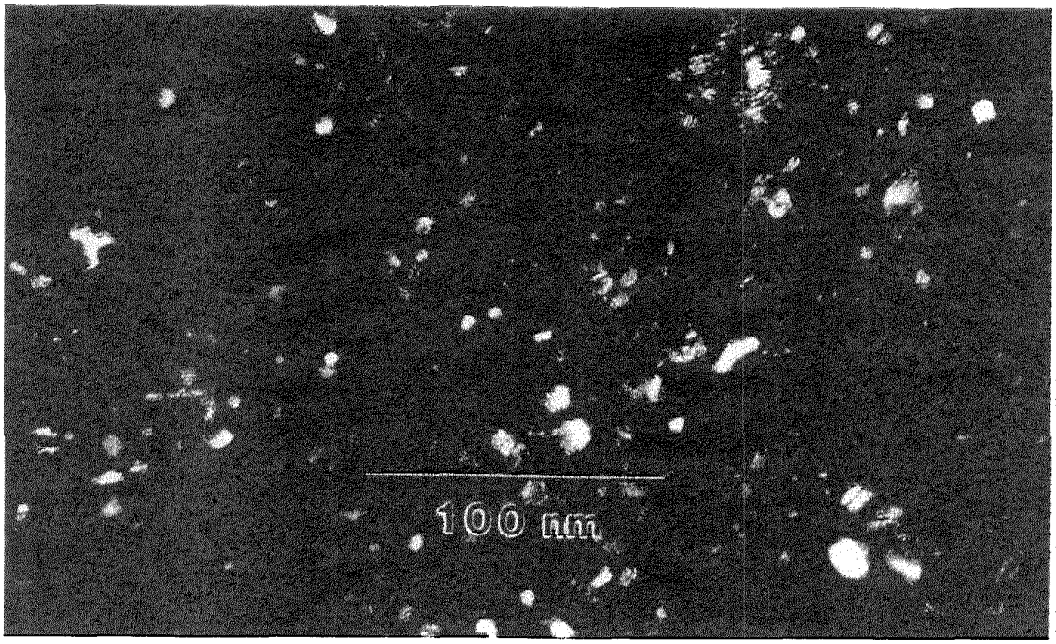

(a) Mo+2Si powder mixture after 16 hours of ball milling.

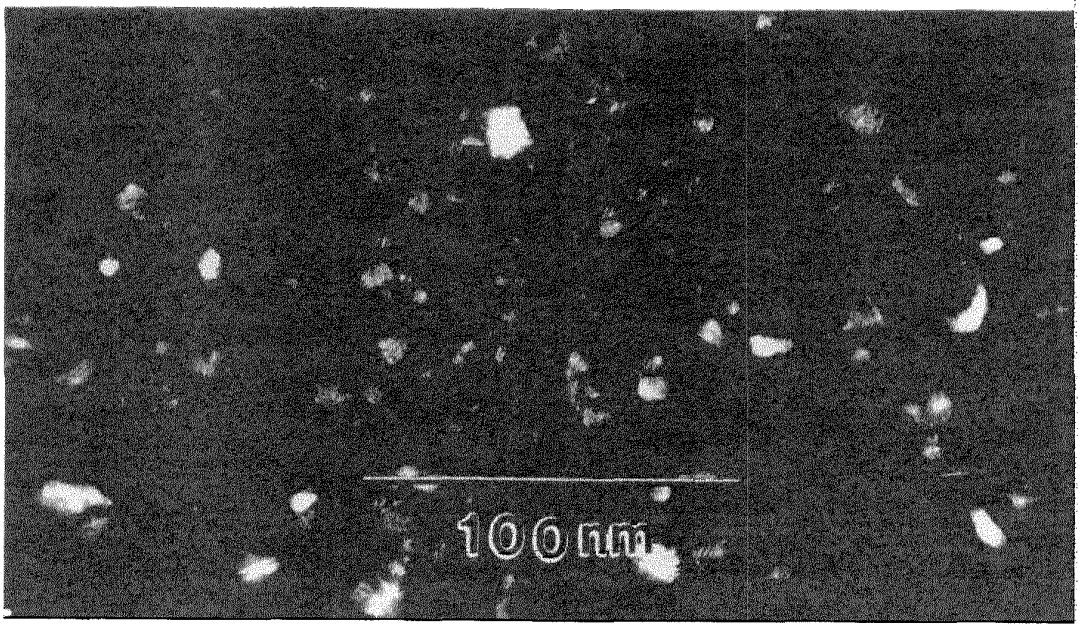

(b) Mo+2Si powder mixture after 144 hours of ball milling.

Figure 4.16 TEM micrograph indicates nanosize formation of $MoSi_2$ particles with variation in grain size.

References:

1. Z.A. Munir, *Ceram. Bull.*, **67**, p. 324 (1988).

2. A.K. Vasudevan, J.J. Petrovic, *Mat. Sci. and Eng.*, **A155**, p. 1 (1992).

3. R.B. Schwarz, S. R. Srinvasan, J.J. Petrovic and C.J. Maggiore, *Mat. Sci. and Eng.*g., **A155**, p. 75 (1992).

4. I.J. Shon, Z.A. Munir, K. Yamazaki, K. Shoda, *J. Am. Ceram. Soc.*, **79** (7), p. 1875 (1996).

5. D. M. Shah, D. Berczik, D.L. Anton and R. Hecht, *Mat. Sci. and Engg.*, **A155**, p. 45 (1992).

6. L. Xiao, Y.S. Kim, R. Abbaschian, *Mat. Sci. Engg.*, **A144**, p. 277 (1991).

7. J. D. Cotton, Y.S. Kim and M.J. Kaufman, *Mat. Sci. Engg.*, **A144**, p. 287 (1991).

8. Y.L. Jeng, E.J. Lavernia, *J. of Mat. Sci.*, **29**, p. 2557 (1994).

9. R.W. Armstrong, *Met. Trans.*, **1**, p. 1170 (1970).

10. T.G. Nieh and J. Wadsworth, *Scripta Metall. Mater.*, **25**, p. 955 (1991).

11. T.B. Massakali, J.L. Murray, L.H. Bennett and H. Baker, *Binary Alloy Phase Diagrams*, American Society for Metals, Metals Park, OH (1986).

12. K. Stahl and R. Thomasson, *J. Appl. Cryst.*, **25**, p. 251 (1992).

13. M. Evain, P. Deniard, A. Jouanneaux and R. Brec, *J. Appl. Cryst.*, **26**, p. 563 (1993).

14. A. Mutz, T. Vreeland, Jr., in *Shock Wave and High-Strain-Rate Phenomena in Materials* (ed. M.A. Meyers, L.E. Murr and K.P. Staudhammer), p. 425 Marcel Dekker, Inc., New York (1992).

15. B.R. Krueger, A.H. Mutz and T. Vreeland, Jr., *Met. Trans.*, **23A**, p. 55 (1992).

16. E. Ma, J. Pagan, G. Cranford, and M. Atzmon, *J. Mater. Res.*, **8** (8), p. 1836 (1993).

17. Private Communication with S. C. Deevi (May 1995).

18. D. L. Zhang, *J. Mat. Sci. Let.*, **14**, p. 1508 (1995).

19. H.P. Klug, L. Alexander, *X-ray Diffraction Procedures for Polycrystalline and Amorphous Materials*, 2nd. ed., John Wiley and Sons, New York (1974).

20. J. Eckert, J.C. Holzer, C.E. Krill,III, W.L. Johnson, *J. Mater. Res.*, **7**, p. 1751 (1992).

21. W.A. Maxwell, in *Proc. Metallurgy and Materials Information Meet.*, Oak Ridge, TN, April 16-18, 1951, Rep. TID-5061 (DEL).

22. M.A. Meyers, S.S. Batsavov, S.M. Gavrilkin, H.C. Chen, J.C. LaSalvia, F.D.S. Marquis, *Mat. Sci. and Eng.*, **A201**, p. 150 (1995).

APPENDIX:

The following is the fortran program code employed to solve for the initial rate of the reaction for the disilide formation ($TiSi_2$) at the molten Si - solid Ti interface. The input file is listed at the end of program.

```
PROGRAM HEAT2
    IMPLICIT DOUBLE PRECISION(A-H,O-Z)
    parameter (maxmat=50000)
    DIMENSION CAPMAT(maxmat), CONDMAT(3,maxmat),T(maxmat),TN(maxmat)

c   Data input A= particle size (cm), NSTEPS = total number of steps, SZ = thickness of molten zone
c   rate = reaction rate, RF = interval of steps to write to data file
    READ(5,*)A,NUMB,NSTEPS,SZ,rate,RF
    NE = 32*NUMB
     !changed fixed number here!
    SS = 16-SZ
      SS1 = 16
c    SS = (SZ-1.)/2.
c    SS1 = SS+1.
    ALE = A/32 /NUMB    !changed ss to 32
    hf = 133000./104.072
    rho = 3.5
       if (33*numb+1.ge.MAXMAT) then
      print *,'increase parameter MAXMAT'
      stop
    endif
    READ(5,*) COND1,RHO1,CP1                    !Thermophysical constant matrix
    READ(5,*) COND2,RHO2,CP2
    READ(5,*) COND3,RHO3,CP3
    HSOURCE = hf*rho*rate

    DT = 0.5 * RHO1*CP1/COND1*ALE**2

C    INPUT INITIAL PROFILE HERE
      write(7,'("s0={")')
    DO I=1,33*NUMB+1
      if (i.le.SS*numb) Tn(i) = 300                          !Initial temperature profile
      if (i.ge.SS*numb+1.and.i.le.SS1*numb+1) Tn(i) = 1685.  !Kelvin
      if (i.gt.SS1*numb+1) Tn(i) = 300.
WRITE(6,'(f22.6)",")')Tn(i)                  !Writing initial profile to output file
        if (i.ne.33*numb+1) then
          write(7,'(f22.6",")')Tn(I)
        else
          write(7,'(f22.6)')Tn(I)
        end if
    END DO

    write(7,'("}")')
```

```
  ! Writing the matrix for the  thermophysical properties for each component
    CAPMAT(1) = RHO1*CP1
    CONDMAT(2,1) = COND1
CONDMAT(1,2) = -COND1
    CONDMAT(3,1) = -COND1

    DO I=2,SS*NUMB
      CAPMAT(I) = 2.*RHO1*CP1
      CONDMAT(2,I) = 2.*COND1
      CONDMAT(1,I+1) = -COND1
      CONDMAT(3,I) = -COND1
    END DO

    CAPMAT(SS*NUMB+1) = RHO1*CP1 + RHO2*CP2
CONDMAT(2,SS*NUMB+1) = COND1+COND2
    CONDMAT(1,SS*NUMB+2) = -COND2
    CONDMAT(3,SS*NUMB+1)   = -COND2

    DO I=SS*NUMB+2,SS1*NUMB
      CAPMAT(I) = 2.*RHO2*CP2
      CONDMAT(2,I) = 2.*COND2
      CONDMAT(1,I+1) = -COND2
      CONDMAT(3,I) = -COND2
    END DO
CAPMAT(SS1*NUMB+1) = RHO3*CP3 + RHO2*CP2
    CONDMAT(2,SS1*NUMB+1) = COND3+COND2
    CONDMAT(1,SS1*NUMB+2) = -COND3
    CONDMAT(3,SS1*NUMB+1) = -COND3

    DO I=SS1*NUMB+2,33*NUMB
      CAPMAT(I) = 2.*RHO3*CP3
      CONDMAT(2,I) = 2.*COND3
      CONDMAT(1,I+1) = -COND3
      CONDMAT(3,I) = -COND3
    END DO

CAPMAT(33*NUMB+1) = RHO3*CP3
    CONDMAT(2,33*NUMB+1) = COND3


    DO I=1,33*NUMB+1
      CAPMAT(I) = CAPMAT(I)*ALE/2.
      DO J=1,3
        CONDMAT(J,I) = CONDMAT(J,I)/ALE
C       PRINT '(3E12.4)',(CONDMAT(J,I),J=1,3)
      END DO
C   writing temperature profile to file
Count=1
    do ipr=1,NSTEPS
     if (count.ne.RF) then   !loop to write to file
     GOTO 30
```

```
tn(i) = t(i)
        end do
      END DO
    end do
    STOP
    END
```

Input data file

75e-4 100 3000 2 400 1000	! Size of particle (cm), multiple of elements, total number of steps, fraction of melt, rate of reaction, interval of steps to write output
0.508 2.33 0.8636	! k,ρ,c_p For Si
0.509 0.220 2.33 1.033	! k,ρ,c_p For Si at Tm
0.197 4.51 0.6775	! k,ρ,c_p For Ti

```
      endif
      if (ipr.lt.10) then
        write(7,'("s"i1"={")')ipr
      else if (ipr.lt.100) then
        write(7,'("s"i2"={")')ipr
      else if (ipr.lt.1000) then
write(7,'("s"i3"={")')ipr
      else if (ipr.lt.10000) then
        write(7,'("s"i4"={")')ipr
      else if (ipr.lt.100000) then
        write(7,'("s"i5"={")')ipr
      end if
      Count=0       !Reset counter
      DO I=1,33*NUMB+1
        if (i.ne.33*numb+1) then
          write(7,'(f22.6",")')T(I)
            else
          write(7,'(f22.6)')T(I)
        end if
      END DO
      write(7,'("}")')
 30   Count=Count+1   !incrementing counter

   DO ITIME=1,10    ! <-- change this
      PRINT *,'TIME:',DT*(ITIME-1),'STEP NUMBER:',ITIME

      DO I=1,33*NUMB+1
        IF (I.NE.1) THEN
          AUX = CONDMAT(3,I-1)*TN(I-1)
ELSE
          AUX = 0.
        END IF
        TERM3 = AUX+CONDMAT(2,I)*TN(I)+CONDMAT(1,I+1)*TN(I+1)
        T(I) = -TERM3*DT
        IF (I.EQ.SS1*NUMB+1) T(I) = T(I) + HSOURCE*DT
        T(I) = T(I)/CAPMAT(I)
        T(I) = T(I) + TN(I)

      END DO
      do i=1,33*NUMB+1
ELSE
          AUX = 0.
        END IF
        TERM3 = AUX+CONDMAT(2,I)*TN(I)+CONDMAT(1,I+1)*TN(I+1)
        T(I) = -TERM3*DT
        IF (I.EQ.SS1*NUMB+1) T(I) = T(I) + HSOURCE*DT
        T(I) = T(I)/CAPMAT(I)
        T(I) = T(I) + TN(I)

      END DO
      do i=1,33*NUMB+1
```